

Hubbard and Heisenberg models on hyperbolic lattices - Metal-insulator transitions, global antiferromagnetism and enhanced boundary fluctuations

Anika Götz,¹ Gabriel Rein,¹ João Carvalho Inácio,¹ and Fakher F. Assaad^{1,2}

¹*Institut für Theoretische Physik und Astrophysik, Universität Würzburg, 97074 Würzburg, Germany*

²*Würzburg-Dresden Cluster of Excellence ct.qmat, Am Hubland, 97074 Würzburg, Germany*

(Dated: June 6, 2024)

We study the Hubbard and Heisenberg models on hyperbolic lattices with open boundary conditions by means of mean-field approximations, spin-wave theory and quantum Monte Carlo (QMC) simulations. For the Hubbard model we use the auxiliary-field approach and for Heisenberg systems the stochastic series expansion algorithm. We concentrate on bipartite lattices where the QMC simulations are free of the negative sign problem. The considered lattices are characterized by a Dirac like density of states, Schläfli indices $\{p, q\} = \{10, 3\}$ and $\{8, 3\}$, as well as by flat bands, $\{8, 8\}$. The Dirac density of states cuts off the logarithmic divergence of the staggered spin susceptibility and allows for a finite U semi-metal to insulator transition. This transition has the same mean-field exponents as for the Euclidean counterpart. In the presence of flat bands we observe the onset of magnetic ordering at any finite U . The magnetic state at intermediate coupling can be described as a global antiferromagnet. It breaks the C_p rotational and time reversal symmetries but remains invariant under combined $C_p\mathcal{T}$ transformations. The state is characterized by macroscopic ferromagnetic moments, that globally cancel. We observe that fluctuations on the boundary of the system are greatly enhanced: while spin wave calculations predict the breakdown of antiferromagnetism on the boundary but not in the bulk, QMC simulations show a marked reduction of the staggered moment on the edge of the system.

I. INTRODUCTION

The effect of dimensionality and point group symmetries on correlation induced phenomena is an established research domain in flat Euclidean space. The aim of this paper is to investigate the effect curvature has on the physics of standard models of correlated electrons and spins. The role of the curvature is widely studied in models of statistical mechanics, like the Ising model [1–8]. A constant negative curvature can for example lead to the presence of symmetry-broken phases and phase transitions, not present in the flat Euclidean plane [1, 2, 9–11] or change the critical properties of phase transitions [3, 5, 12]. Also in condensed matter physics the popularity of hyperbolic lattices is increasing. The topics of interest are both single-particle physics, like the electronic band structure [13–27] – also under the influence of a magnetic field and topological phenomena – and correlation effects [26, 28, 29]. The motivation can partially be attributed to recent experimental realizations of hyperbolic lattices in circuit quantum electrodynamics and electric circuits [30, 31].

In this paper we study the Hubbard and Heisenberg models on three exemplary regular tessellations of the hyperbolic plane, that exhibit different electronic properties in the non-interacting limit. We use a Hartree-Fock approximation, a spin wave analysis, auxiliary-field and stochastic series expansion quantum Monte Carlo (QMC) methods to investigate the models as a function of the interaction strength and system size. Since all considered lattices are bipartite, we can perform QMC simulations without a negative sign problem for both the Hubbard and Heisenberg models.

The electronic properties of the three lattices resem-

ble a Dirac system with a linear density of states (DOS) around the Fermi level ($\{10, 3\}$ and $\{8, 3\}$ lattice), and a flat-band system with a high DOS at the Fermi level ($\{8, 8\}$ lattice). The mean-field approximation of the Hubbard model on the $\{10, 3\}$ lattice is already studied in Ref. [26], and we complement these results with both spin wave calculations and first-time fermionic QMC studies on the hyperbolic lattice. We will compare the spatial distribution of the magnetic ordering in the weak-coupling and strong-coupling limits, the transition from a semi-metal to insulator with antiferromagnetic (AFM) ordering as a function of the interaction strength and thermodynamic properties.

The remainder of the paper is organized as follows. In Sec. II we define the Hubbard and Heisenberg models and the hyperbolic lattices on which we study them. In Sec. III we introduce the mean-field approximation, spin-wave analysis and the QMC algorithms that will be used in this work. In Sec. IV we present our numerical results before we conclude in Sec. V. In the Appendix additional numerical data can be found.

II. HYPERBOLIC LATTICES, HUBBARD AND HEISENBERG MODELS

A. Hyperbolic lattices

In this work, we consider two-dimensional graphs that can be categorized by their Schläfli index $\{p, q\}$. The lattice sites are located at the corners of regular p -gons and every lattice site has coordination number q [32]. Hyperbolic lattices with a constant negative curvature fulfill the condition $(p - 2)(q - 2) > 4$. In contrast, lattices

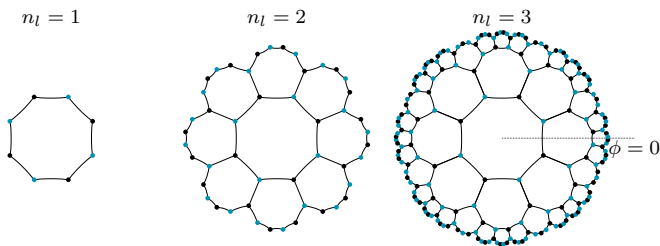


FIG. 1. $\{8, 3\}$ lattice in the Poincaré disk model with increasing number of layers n_l . Reference angle marked for latter use.

with $(p-2)(q-2) = 4$ lie within the flat Euclidean plane and lattices with $(p-2)(q-2) < 4$ in a positively curved plane. For the Euclidean plane exactly three solutions exist – the square lattice $\{4, 4\}$, the honeycomb lattice $\{6, 3\}$ and the triangular lattice $\{3, 6\}$, whereas for the hyperbolic case infinitely many pairs $\{p, q\}$ exist that fulfill the condition [33].

We concentrate on finite size hyperbolic lattices with open boundary conditions. The lattice size can be increased by starting with a single p -gon and successively adding shells or layers of p -gons. The number of lattice sites grows exponentially with the number of layers, strongly limiting the accessible lattice sizes for our calculations. In Fig. 1 the $\{8, 3\}$ lattice is shown with up to $n_l = 3$ layers. In order to properly depict the lattices, the Poincaré disk model is used. All lattice sites are projected into the open unit disk and all edges, connecting two nearest-neighboring sites, are geodesic lines. Those geodesics are circular arcs in the Poincaré disk model, that would hit the unit circle perpendicular and they all have the same length within the hyperbolic metric [34] [35, 36].

Drawing conclusions from the results on finite lattices about the properties in the thermodynamic limit is somewhat more complicated than in the Euclidean plane. For open boundary conditions the ratio of lattice sites at the edge to the total number of lattice sites converges to a finite value, so the behavior of the edge sites is not negligible even for large system sizes [3, 6, 24, 27]. If the bulk properties are of interest, the lattice can be successively increased and the calculation can only be done for the inner bulk part, neglecting the outer shells [3, 4]. Another possibility is to use periodic boundary conditions. Some classes of hyperbolic tilings can be placed on compact surfaces with higher genus $g \geq 2$ with periodic boundary conditions [8, 18, 19, 28, 37]. But in this work we use open boundary conditions and also take into account the boundary contributions.

Fig. 1 also shows, that the $\{8, 3\}$ lattice is bipartite with sublattice A and B , like all lattices in this work. In general for even p the resulting lattices are bipartite [27]. In Table I of the Appendix we provide a list of the considered lattice sizes and their respective number of lattice sites N_s .

B. Hubbard and Heisenberg models

The Hamiltonian of the Hubbard model is given by [38–40]

$$\begin{aligned} \hat{H} &= \hat{H}_t + \hat{H}_U, \\ \hat{H}_t &= -t \sum_{\langle i, j \rangle} \sum_{\sigma=1}^{N_\sigma} \left(\hat{c}_{i, \sigma}^\dagger \hat{c}_{j, \sigma} + \text{h.c.} \right), \\ \hat{H}_U &= \frac{U}{N_\sigma} \sum_i \left(\sum_{\sigma=1}^{N_\sigma} \hat{n}_{i, \sigma} - \frac{N_\sigma}{2} \right)^2. \end{aligned} \quad (1)$$

The first term describes the hopping of fermions on bonds $b = \langle i, j \rangle$ connecting nearest-neighboring sites i and j with hopping strength t . The operator $\hat{c}_{i, \sigma}^\dagger$ creates a fermion in a Wannier state centered at site i and with z component of spin equal to σ . We will consider $N_\sigma = 2$ (spin $S = \frac{1}{2}$) flavored fermions. The fermions interact via a repulsive on-site Hubbard potential with strength U , as described in the second term.

The model is symmetric under global $SU(2)$ rotations with the spin operators as the generators of the group

$$\hat{S}^\alpha = \frac{1}{2} \sum_{i, \sigma, \sigma'} \hat{c}_{i, \sigma}^\dagger \sigma_{\sigma, \sigma'}^\alpha \hat{c}_{i, \sigma'}. \quad (2)$$

Here $\sigma^{\alpha=x, y, z}$ are the three Pauli matrices. Furthermore, the model is invariant under particle-hole transformations $\hat{P}^{-1} \hat{c}_{i, \sigma}^\dagger \hat{P} = (-1)^i \hat{c}_{i, \sigma}$ on a bipartite lattice at half-filling. The prefactor $(-1)^i$ is a multiplicative phase factor, that takes the value $+1$ on sublattice A and -1 on sublattice B .

The lattice geometry can significantly influence the electronic band structure and therefore the behavior of the electrons, when exposed to interactions. This effect can be observed for the available regular bipartite graphs in the Euclidean plane, the square lattice $\{4, 4\}$ and the honeycomb lattice $\{6, 3\}$. On both lattices the repulsive Hubbard model at half-filling undergoes a transition from a (semi-)metal to an AFM insulator in the limit of strong on-site interactions. The Fermi surface of the half-filled square lattice exhibits van Hove singularities leading to a logarithmically divergent DOS at the Fermi surface. This results in an essential singularity of the staggered magnetization in the Hartree-Fock approximation, meaning that for any finite interaction strength U the AFM state is expected to have a lower energy than the paramagnetic solution [41, 42]. Numerical studies support the presence of long-range AFM order for any finite interaction U [41, 43–45].

On the honeycomb lattice the band structure of the non-interacting case exhibits two Dirac cones and the Fermi surface is concentrated on two points with a vanishing DOS. A finite critical on-site repulsion U_c is needed for the formation of long-range AFM ordering [46]. Numerical studies locate a continuous and direct semi-metal

to insulator transition at $U_c/t \approx 3.8$ [47–49]. This transition belongs to the Gross-Neveu universality class [48–50].

For the hyperbolic case we know, that the unique ground state of the half-filled repulsive Hubbard model is a $S_{\text{tot}} = 0$ state for any bipartite lattice by a theorem of Lieb [51]. S_{tot} is the total spin and the theorem was proven for any bipartite collection of sites, meaning no explicit periodicity or dimensionality is assumed in the proof of the theorem. Furthermore in the strong-coupling limit the model maps onto the Heisenberg model with an AFM coupling [52], since the mapping is independent of the lattice. The specific form of the model reads:

$$\hat{H} = J \sum_{\langle i,j \rangle} \hat{S}_i \cdot \hat{S}_j \quad (3)$$

with $J = \frac{4t^2}{U}$ and $\hat{S}_i = \frac{1}{2} \sum_{\sigma,\sigma'} \hat{c}_{i,\sigma}^\dagger \boldsymbol{\sigma}_{\sigma,\sigma'} \hat{c}_{i,\sigma'}$.

III. METHODS

A. Mean-field approximation

As a first approach to study the Hubbard model on hyperbolic lattices we choose a mean-field approximation. We decouple the electron-electron interaction by coupling the z component of the spin operator to the fields ϕ_i

$$\hat{H}_{\text{MF}} = \hat{H}_t - U \sum_i \phi_i (\hat{n}_{i,\uparrow} - \hat{n}_{i,\downarrow}) + \frac{U}{2} \sum_i \phi_i^2, \quad (4)$$

$$\phi_i = \langle \hat{n}_{i,\uparrow} - \hat{n}_{i,\downarrow} \rangle_\phi = 2 \langle \hat{S}_i^z \rangle_\phi = m_i^z, \quad (5)$$

where $\langle \dots \rangle_\phi = \frac{\text{Tr}[\dots e^{-\beta \hat{H}_{\text{MF}}}]}{\text{Tr}[e^{-\beta \hat{H}_{\text{MF}}}]}$ is the expectation value with respect to \hat{H}_{MF} and $\beta = T^{-1}$ the inverse temperature. The fields ϕ_i are equivalent to the local magnetic order parameter and due to the absence of translation symmetry in the considered lattices, we allow the fields to vary from site to site. In the following, Eq. (5) will be solved self-consistently. In Appendix C we show that, due to particle-hole symmetry, the staggered spin susceptibility diverges logarithmically in the low-temperature limit, the prefactor being the DOS at the Fermi energy. Hence, we foresee AFM ordering and define the staggered order parameter

$$m^z = \frac{1}{N_s} \sum_i (-1)^i m_i^z. \quad (6)$$

B. Spin wave approximation

We continue with a spin wave approximation. In the strong-coupling limit the Hubbard model maps onto the

AFM Heisenberg model independently of the lattice geometry [52]

$$\hat{H} = \sum_{\langle i,j \rangle} \hat{S}_i \cdot \hat{S}_j = \frac{1}{2} \sum_{i,j} T_{i,j} \hat{S}_i \cdot \hat{S}_j. \quad (7)$$

The matrix T is the adjacency matrix of the lattice with $T_{i,j} = 1$, if sites i and j are nearest neighbors and $T_{i,j} = 0$ otherwise. Following Ref. [53], we use a Holstein-Primakoff transformation to map the spin operators \hat{S}_i to boson operators \hat{b}_i^\dagger and expand in $\frac{1}{S}$. Since we start from an AFM, we choose on sublattice A the representation

$$\hat{S}_i^z = S - \hat{b}_i^\dagger \hat{b}_i, \quad \hat{S}_i^+ = \hat{S}_i^x + i \hat{S}_i^y = \sqrt{2S} \hat{b}_i \quad (8)$$

and on sublattice B

$$\hat{S}_i^z = \hat{b}_i^\dagger \hat{b}_i - S, \quad \hat{S}_i^+ = \sqrt{2S} \hat{b}_i^\dagger. \quad (9)$$

The correction to the classically expected Néel state is given by the expectation value of the bosonic occupation number $\langle \hat{b}_i^\dagger \hat{b}_i \rangle$. In Appendix B we sketch the calculation of the site-dependent correction.

C. Quantum Monte Carlo

In order to acquire deeper information about the electronic correlations on the various lattice geometries and support the mean-field and spin wave data, we employ QMC studies as our secondary approach. In the weak-coupling limit, we use a finite-temperature version of the auxiliary-field QMC (AFQMC) method to simulate the Hubbard model [44, 54, 55]. For the strong-coupling regime, the Hubbard model is mapped to an AFM Heisenberg model, and in this regime we use the Stochastic Series Expansion (SSE) method with directed loop updates [56, 57].

1. Auxiliary-field QMC

We use the Algorithms for Lattice Fermions (ALF) [58] implementation of the finite-temperature AFQMC algorithm [44, 54, 55]. It allows us to accurately simulate the model in various parameter regimes. As for the Hubbard model at half-filling, our simulations do not suffer from the negative sign problem.

Although the construction of momentum space, similar to Euclidean lattices, is possible [16, 18, 19], it does not apply to our lattices with open boundary conditions due to the absence of translation invariance and we have no notion of momentum space. Yet, the QMC algorithm can be employed to calculate the uniform susceptibility

$$\chi_o = \frac{\beta}{N_s} \sum_{i,j} \left(\langle \hat{O}_i \hat{O}_j \rangle - \langle \hat{O}_i \rangle \langle \hat{O}_j \rangle \right) \quad (10)$$

at nonzero Hubbard- U with \hat{O}_i being either density $\hat{n}_i = \sum_{\sigma} \hat{n}_{i,\sigma}$ or spin operators \hat{S}_i^z . To directly compare the QMC results with mean-field, we make use of the bipartite nature of the chosen lattices by constructing an AFM order parameter as

$$m_{\text{AFM}}^z = \sqrt{\frac{1}{N_s^2} \sum_{i,j}^{N_s} (-1)^i (-1)^j \langle \hat{S}_i^z \hat{S}_j^z \rangle}, \quad (11)$$

which is directly related to the spin-spin-correlation function. For all of the presented data, we used a code for the Hubbard model with SU(2)-decoupling and an imaginary time discretization of $\Delta\tau t = 0.1$ [58].

2. Stochastic Series Expansion

As a second QMC approach, we simulate the Heisenberg model on the hyperbolic lattices using the SSE method with directed loop updates [56, 57]. Since the considered lattices are of bipartite nature, the method can be formulated without a sign problem. This approach allows us to access larger lattice sizes compared to the AFQMC method, since SSE simulations scale as $\mathcal{O}(\beta N_s)$ as opposed to $\mathcal{O}(\beta N_s^3)$ [58].

The SSE method is based on the Taylor expansion of the partition function Z in some complete basis $\{|\alpha\rangle\}$ (here we choose the S^z -basis)

$$Z = \sum_{\alpha} \sum_{n=0}^{\infty} \sum_{S_n} \frac{(-\beta)^n}{n!} \langle \alpha | \prod_{i=1}^n H_{a_i, b_i} | \alpha \rangle, \quad (12)$$

n is the current expansion order, S_n specifies the operator string $[(a_1, b_1), \dots, (a_n, b_n)]$ and H_{a_i, b_i} is a bond term of the Hamiltonian which operates on bond b_i . This action can be diagonal or off-diagonal depending on a_i . The configuration space then consists of operator strings of varying size n . To sample this space, we use two main types of updates. Diagonal updates are a local type of update, in which we insert/remove a Hamiltonian operator in S_n . The directed loop update [57, 59] is a global type of update in which a loop is constructed and flipped in the vertex representation of S_n , allowing us to change a large part of the configuration in one step.

Both the uniform spin susceptibility [Eq. (10)] and the AFM order parameter [Eq. (11)] rely on the calculation of equal-time two-point spin correlations $\langle \hat{S}_i^z \hat{S}_j^z \rangle$. As these operators are diagonal in the S^z -basis, their evaluation within the SSE formalism is trivial.

IV. RESULTS

In the following we study the SU(2) spin symmetric Hubbard and Heisenberg models on three different hyperbolic lattice geometries at the particle-hole symmetric point. As shown in Appendix C particle-hole symmetry leads to a logarithmic divergence of the staggered

spin susceptibility, provided that the DOS is finite at the Fermi energy. Hence, the first question that we will address in Sec. IV A is the DOS in the non-interacting limit. In Sec. IV B we present and discuss our mean-field results. In Sec. IV C, we then systematically take into account fluctuations with a spin wave approximation for the Heisenberg model, and numerically exact QMC simulations for both models.

A. Non-interacting limit $U = 0$

First we consider the DOS of the $\{10, 3\}$ lattice,

$$\rho(E) = -\frac{1}{\pi N_s} \sum_n \text{Im} G^R(n, E). \quad (13)$$

The retarded Green function is given by $G^R(n, E) = \frac{1}{E - E_n + i\delta}$ with an infinitesimal δ and E_n are the discrete energy eigenstates of the tight-binding Hamiltonian \hat{H}_t . Since our Hamiltonian enjoys particle-hole symmetry, the DOS is symmetric around $E = 0$ and the chemical potential for half-band filling is pinned to zero for all temperatures. The uniform spin susceptibility χ_S , defined in Eq. (10), is given by

$$\chi_S = -(2S + 1) \int dE \rho(E) \frac{\partial f(E)}{\partial E} \quad (14)$$

for the free case. In the above, f denotes the Fermi-function. Both the DOS and the uniform spin susceptibility are plotted in Fig. 2(Ia) and 2(IIa). The data, in the limit of large values of n_l , is consistent with a DOS $\rho(E) \propto |E|$ and a corresponding uniform spin susceptibility $\chi_S \propto T$. The DOS close to the Fermi level as well as the uniform spin susceptibility bear similarities with Dirac systems.

In Figs. 2(Ib) and 2(IIb) we consider the $\{8, 3\}$ lattice. At even number of layers, there are no zero-energy eigenstates in the spectrum and χ_S decreases exponentially in the low-temperature limit. The activation gap can be attributed to the finite-size gap. On the other hand, for an odd number of layers exactly two eigenstates at zero energy are present, thereby resulting in a T^{-1} law of the uniform spin susceptibility in the low-temperature limit. But as the number of layers is increased the ratio of zero-energy eigenstates to the total number of eigenstates quickly converges to zero and the magnitude of the T^{-1} law vanishes in the large n_l limit. We note that the slope of the DOS around $E = 0$ and of the spin susceptibility is steeper for the $\{8, 3\}$ lattice compared to the former lattice. In Euclidean space, the slope is given by the inverse of the Fermi velocity.

The $\{8, 8\}$ lattice on the other hand shows flat band features on the considered finite lattices. A large number of energy eigenstates are located at zero energy [Fig. 2(Ic)] and the uniform spin susceptibility diverges in the zero temperature limit [Fig. 2(IIc)]. As mentioned

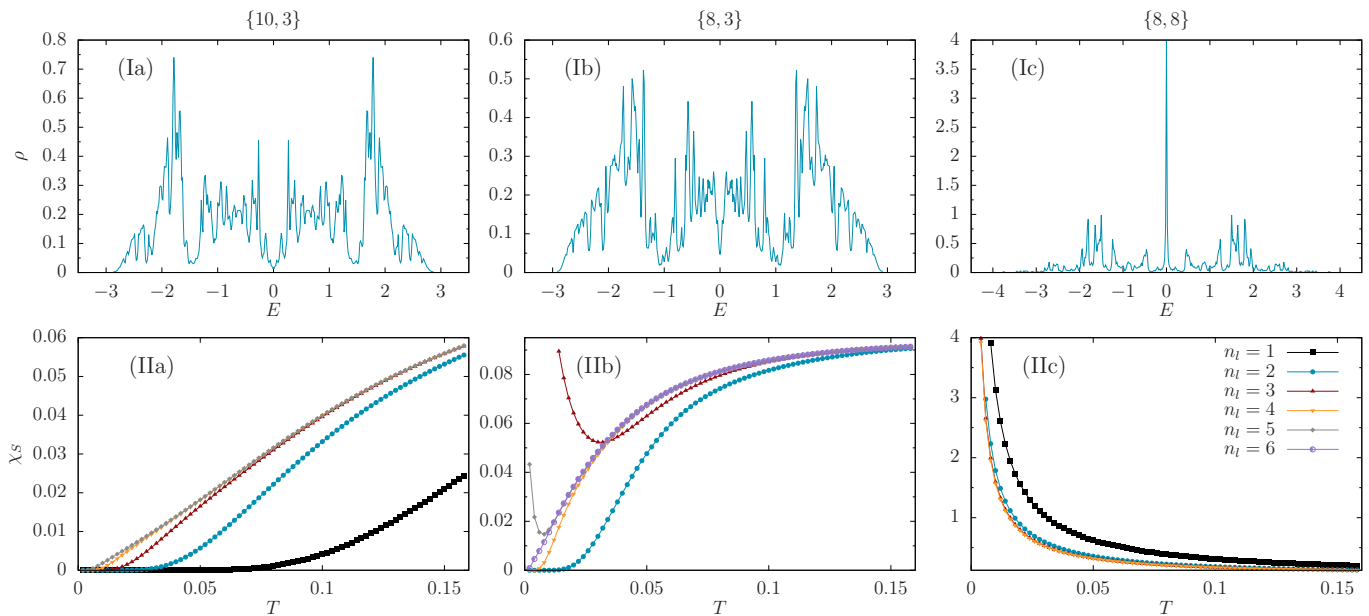


FIG. 2. (Ia)-(Ic) DOS $\rho(E)$ as a function of the energy E at $\delta = 0.01$ for the largest considered lattice sizes ($n_l = 5$ for the $\{10, 3\}$ lattice, $n_l = 6$ for $\{8, 3\}$ and $n_l = 4$ for $\{8, 8\}$, see also Table I) and (IIa)-(IIc) uniform spin susceptibility χ_S as a function of the temperature T and the number of layers n_l in the non-interacting case $U = 0$.

previously, the boundary of hyperbolic lattices has an extensive number of sites such that the bulk, Ref. [27], and total DOS, Eq. (13) can differ. Comparing results, we see that the flat band observed in the $\{8, 8\}$ lattice is boundary induced.

B. Mean-field approximation

1. Staggered magnetization and metal-insulator transition

In this section we study the three lattice systems with the mean-field approximation, introduced in Sec. III A. Figure 3 shows the order parameter as a function of the interaction strength U . In the strong-coupling limit a clear AFM state develops for all lattices with a vanishing total spin and a strong AFM moment m^z . The insets of Fig. 3 show the local magnetic moment m_i^z , with a nearly spatially uniform modulus $|m_i^z|$, deep in the AFM phase at $U = 5t$.

The behavior of the three lattices in the weak-coupling limit differ strongly as a consequence of the DOS in the non-interacting case. In fact in Appendix C we show, that for a finite DOS at the Fermi level and under the assumption of partial particle-hole symmetry an instability towards AFM can be expected even in the absence of translational symmetry.

For the Dirac-like $\{10, 3\}$ lattice the order parameter m^z picks up a nonzero value only above a critical interaction strength $U_c \approx 0.76t$. Below U_c the paramagnetic state is energetically favorable. Hartree-Fock mean-field theory for the flat honeycomb lattice predicts a linear

increase of the order parameter above the critical interaction $m^z \propto (U - U_c)$, i.e. a critical exponent of $\beta = 1$ [46, 60, 61]. The order parameter of the $n_l = 4$ lattice is well described by a linear fit close to the critical point [Fig. 3(a)].

The order parameter on the $\{8, 3\}$ exhibits clear odd-even effects in n_l . Let us consider the $n_l = 1$ lattice, that corresponds to the p -site ring with $p = 8$. Since the rotational symmetry of the ring is shared by the $n_l > 1$ lattices, a symmetry analysis will prove to be very useful. The ground state of the $p = 8$ site ring is four-fold degenerate:

$$|\pm, \sigma\rangle = \hat{c}_{k=\pm\frac{\pi}{2}, \sigma}^\dagger |0\rangle. \quad (15)$$

In the above $|0\rangle$ is the non-degenerate ground state of the 8-site ring occupied with six electrons, and $\hat{c}_{k, \sigma}^\dagger = \frac{1}{\sqrt{p}} \sum_{j=1}^p e^{ikj} \hat{c}_{j, \sigma}^\dagger$. Under time-reversal symmetry, \mathcal{T} , and C_8 rotations the states transform as

$$\mathcal{T}|\pm, \sigma\rangle = (i\sigma^y)_{\sigma, \sigma'} |\mp, \sigma'\rangle \quad (16)$$

and

$$C_8|\pm, \sigma\rangle = e^{\pm i\frac{\pi}{2}} |\pm, \sigma\rangle. \quad (17)$$

In the presence of AFM ordering, time-reversal and C_8 symmetries are individually broken, but the combined $C_8\mathcal{T}$ symmetry is conserved. Terms such as

$$\Delta \sum_{\sigma} \sigma [|+, \sigma\rangle \langle -, \sigma| + |-, \sigma\rangle \langle +, \sigma|] \quad (18)$$

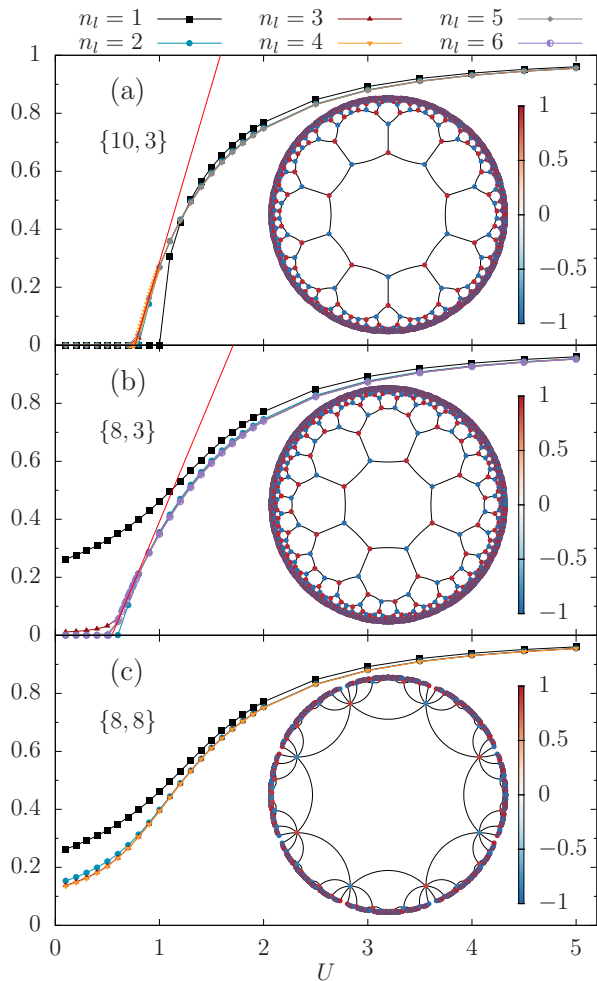


FIG. 3. (a)-(c) AFM order parameter m^z as a function of the interaction strength U . The red line in (a) is a linear fit to the $n_l = 4$ data of the $\{10, 3\}$ lattice close to the critical point $U_c \approx 0.76t$ and in (b) to the $n_l = 6$ data close to $U_c \approx 0.54t$. Insets: local order parameter m_i^z at $U = 5.0t$ for (a) $n_l = 4$, (b) $n_l = 5$ and (c) $n_l = 4$.

are allowed and will lift the ground state degeneracy, yielding

$$|\Psi_0\rangle = \frac{1}{2} (|+, \uparrow\rangle + |-, \uparrow\rangle) \otimes (|+, \downarrow\rangle - |-, \downarrow\rangle). \quad (19)$$

This state has a finite staggered magnetization m^z for any value of Δ , and is symmetric under combined $C_3\mathcal{T}$ symmetries. The jump in the magnetization observed at $n_l = 1$ is a consequence of the degeneracy of the non-interacting ground state and the concomitant divergence of the uniform spin susceptibility.

While the symmetry analysis will apply to arbitrary values of n_l , the degeneracy only occurs for odd values of n_l . Since the degeneracy is intensive, the jump in the staggered magnetization will be suppressed as a function of n_l . For even values of n_l the finite size gap leads to a finite value of U beyond which magnetic ordering will occur.

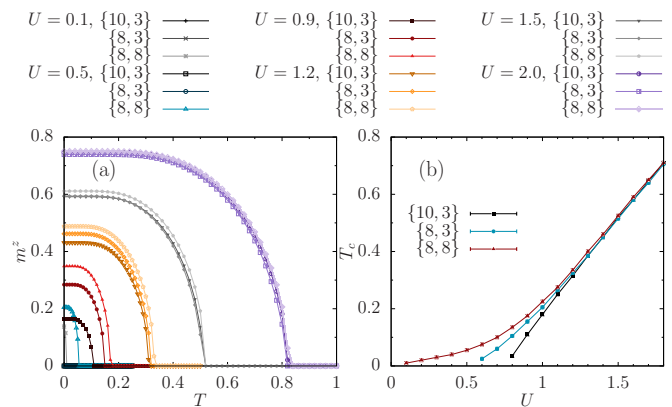


FIG. 4. (a) AFM order parameter m^z as a function of the temperature T for different interaction strengths as obtained from the mean-field approximation. (b) Critical temperature T_c as a function of the Hubbard interaction U . For the $\{10, 3\}$ and $\{8, 8\}$ lattices we chose $n_l = 3$ layers and for the $\{8, 3\}$ lattice $n_l = 4$ layers.

In the large n_l limit we conjecture a Dirac-like system. The—in comparison to the $\{10, 3\}$ lattice lower—critical interaction strength, that lies within the range of $U_c \simeq 0.5t - 0.6t$, is consistent with the observation of Sec. IV A, that the slope of the DOS around $E = 0$ and of the uniform spin susceptibility of the $\{8, 3\}$ lattice is steeper than the one of the $\{10, 3\}$ lattice. Mean-field analysis for a Dirac system in flat space predicts a linear proportionality $U_c \propto v_F$ [61].

In Fig. 4(a) we present the AFM order parameter as a function of temperature T , and Fig. 4(b) the critical temperature as a function of the interaction strength. For the Dirac-like systems our data is consistent with $m^z \propto (T - T_c)^{1/2}$, in the vicinity of T_c and $T_c \propto (U - U_c)$, in the vicinity of U_c . These forms are precisely the same as obtained for Dirac systems on Euclidean lattices. Hence at the mean-field level the semi-metal to insulator transition in hyperbolic and flat spaces are identical.

In contrast the flat-band-like $\{8, 8\}$ lattice immediately supports AFM ordering for any finite U due to the large DOS at the Fermi level in the non-interacting limit. The singularity at $U = 0$ for all considered values of n_l can be traced back to the divergence of the uniform spin susceptibility and accompanying extensive ground state degeneracy. Although the $T = 0$ magnetization is singular at $U = 0$ the Néel transition temperature seems to follow a powerlaw [Fig. 4]) as for other flat band systems [62]. In particular $\lim_{T \rightarrow 0} \lim_{U \rightarrow 0} m^z = 0$, but $\lim_{U \rightarrow 0} \lim_{T \rightarrow 0} m^z > 0$.

2. Global antiferromagnetism

Using the $\{8, 3\}$ lattice as an example, we now concentrate on the weak-coupling limit, meaning that the interaction is (much) smaller than the electronic bandwidth in the non-interacting limit. Fig. 5(a) shows the energy

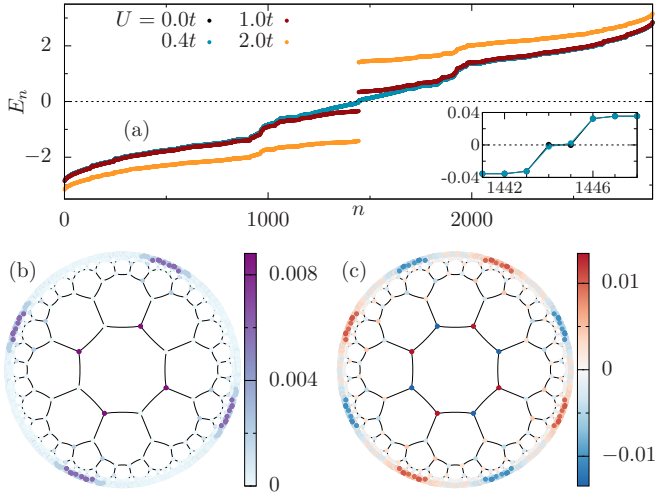


FIG. 5. (a) Energy eigenvalues E_n as obtained from the self-consistent solution of the mean-field Hamiltonian (4), inset: close-up of the Fermi level at $E_n = 0$, (b) absolute value of the wave function of zero mode $|\psi_{n=1444}(\mathbf{i})|^2$ at $U = 0.001t$ and $\sigma = \uparrow$ and (c) magnetization m_i^z at $U = 0.4t$ for the $\{8,3\}$ lattice with $n_l = 5$ layers.

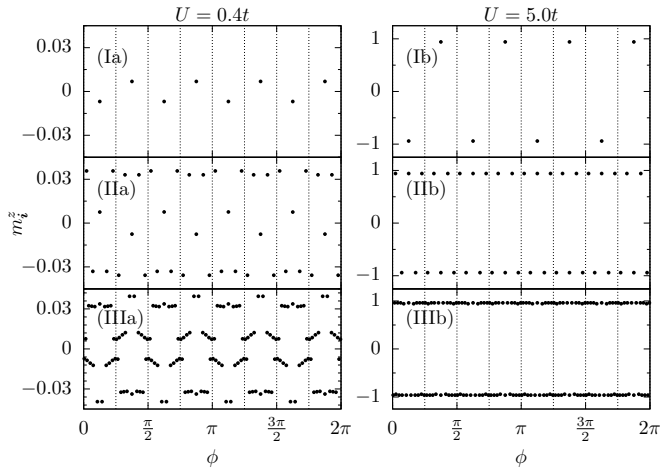


FIG. 6. Local magnetization m_i^z as obtained from mean-field approximation as a function of the angle ϕ at two different interaction strengths (a) $U = 0.4t$ and (b) $U = 5t$ for the $\{8,3\}$ lattice with $n_l = 3$. For clarity all sites of one layer are in a separate plot [(I) layer 1, (II) layer 2 and (III) layer 3].

eigenvalues of the self-consistent solution of the mean-field Hamiltonian (4) for the $\{8,3\}$ lattice with $n_l = 5$ layers and different interaction strengths U . In the non-interacting limit the spectrum is gapless with exactly two zero-energy eigenstates. As for the $n_l = 1$ case, the wave function of a single zero mode, depicted in Fig. 5(b), shows broken C_8 symmetry. Turning on a finite interaction opens a gap, [inset of Fig. 5(a)] and the AFM order parameter acquires a finite value.

As for the $n_l = 1$ case, a small interaction strength of e.g. $U = 0.4t$ affects mainly the two eigenstates at the Fermi level [inset of Fig. 5(a)]. Figure 5(b) shows the

absolute value of the wave function $|\psi_n(\mathbf{i})|^2$ of one zero mode in real-space. In order to lift the degeneracy of the zero modes and have a uniquely defined pattern of the wave function, we choose a small interaction strength of $U = 0.001t$ in Fig. 5(b). The wave function has support only on a small number of sites and it breaks the $C_{p=8}$ symmetry of the lattice down to $C_{p/2=4}$. The wave function of the second zero mode is similar, but rotated by $\pi/4$.

The spatial distribution of the order parameter m_i^z follows the pattern of these wave functions [Fig. 5(c)]. In particular, at finite U the ground state is unique, breaks time-reversal and C_8 symmetries, but satisfies:

$$C_8 \mathcal{T} |\Psi_0\rangle = |\Psi_0\rangle. \quad (20)$$

For the $n_l = 1$ case, this just results in AFM, since the C_8 transformation amounts to a unit translation along the chain. For $n_l > 1$, new magnetic structures emerge, that we will identify with global AFM in these hyperbolic lattices as seen e.g. in strained graphene [63].

First of all, the total magnetic moment vanishes. However, the vanishing of this moment involves cancellation of extensive ferromagnetic moments on each p -th sector of the lattice. This is depicted in Fig. 6, where the local magnetization m_i^z is plotted as a function of the angle ϕ in the different layers, both in the weak $U = 0.4t$ and strong-coupling limit $U = 5t$ for the $\{8,3\}$ lattice with $n_l = 3$ layers. In the strong-coupling limit the magnetization is almost uniform on the whole lattice. At weak coupling the magnetization varies strongly with the angle. Summing over all sites included in $\phi \in [0, \pi/4[$ produces a net positive result, i.e. a ferromagnetic moment that cancels with the contribution of the sites included in $\phi \in [\pi/4, \pi/2[$. The effect is very prominent for the $\{8,3\}$ lattice with $n_l = 5$ layers [Fig. 5(c)], but we observed similar effects in other lattice geometries as well, also in the absence of zero modes [see Appendix D 1 for more examples].

It is tempting to identify our magnetic system as an altermagnet [64]. A corner stone of an altermagnet is compensated magnetism with spin-split bands. We can use the C_p symmetry to identify a unit cell, i , with an orbital structure and corresponding Brillouin zone. Using this notation, the fermion creation operator can be written as $\hat{c}_{i,n,\sigma}^\dagger$ where n denotes orbital n in unit cell i . In this notation, the mean-field Hamiltonian reduces to:

$$\begin{aligned} \hat{H}_{MF} = & \sum_{i,i',n,n',\sigma} \hat{c}_{i,n,\sigma}^\dagger T_{n,n}(i-i') \hat{c}_{i',n',\sigma} \\ & + \sum_{i,n,n',\sigma} \sigma (-1)^i \hat{c}_{i,n,\sigma}^\dagger M_{n,n'} \hat{c}_{i,n',\sigma}. \end{aligned} \quad (21)$$

In the above M is a diagonal matrix that encodes the site magnetization in the unit cell. The factor $(-1)^i$ accounts for the global AFM. We can now carry out a Fourier

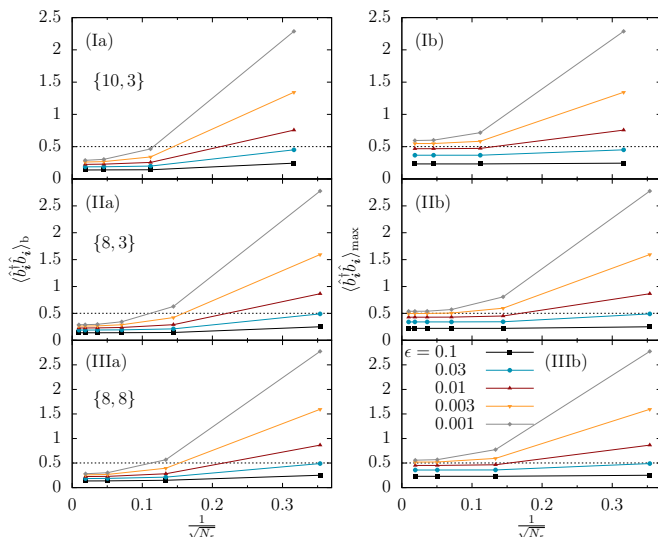


FIG. 7. (a) Average correction $\langle \hat{b}_i^\dagger \hat{b}_i \rangle_b$ of the $n_l - 1$ inner layers and (b) maximal correction $\langle \hat{b}_i^\dagger \hat{b}_i \rangle_{\max}$ as a function of the system size $1/\sqrt{N_s}$ at different strengths ϵ of the infinitesimal staggered field for the (I) {10, 3}, (II) {8, 3} and (III) {8, 8} lattice.

transformation to obtain:

$$\hat{H}_{MF} = \sum_{k \in \text{MBZ}, \sigma} \begin{pmatrix} \hat{c}_{k, \sigma}^\dagger & \hat{c}_{k+Q, \sigma}^\dagger \end{pmatrix} \begin{pmatrix} T(k) & \sigma M \\ \sigma M^\dagger & T(k+Q) \end{pmatrix} \begin{pmatrix} \hat{c}_{k, \sigma} \\ \hat{c}_{k+Q, \sigma} \end{pmatrix} \quad (22)$$

In the above Q is the one-dimensional AFM wave vector, MBZ refers to the magnetic Brillouin zone and $\hat{c}_{k, \sigma}^\dagger$ is a spinor accounting for the orbital degrees of freedom. Using the determinant identity based on the Schur complement, one will readily show that the energy spectrum does not depend on the spin index. As such, we cannot understand the observed global AFM in terms of an altermagnet.

C. Beyond the mean-field approximation

We now consider approximate as well as numerically exact methods that take into account fluctuations. We will first start with the spin wave theory of the Heisenberg model on hyperbolic lattices, and then use Monte Carlo methods for both the Hubbard and Heisenberg models.

1. Spin waves

The motivation to carry out this calculation stems from the fact that the majority of sites on the boundary of the hyperbolic lattice have a coordination number of two akin to a one-dimensional chain. We hence foresee

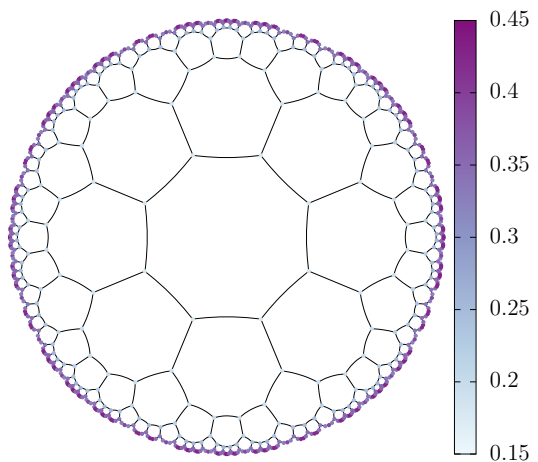


FIG. 8. Local correction $\langle \hat{b}_i^\dagger \hat{b}_i \rangle$ to classical Néel state as obtained from spin wave approximation for the {8, 3} lattice with $n_l = 4$ at $\epsilon = 0.01$.

that fluctuations on the edge will be greatly enhanced. To carry out the calculation we follow Refs. [65, 66], where spin-wave calculations were formulated for spin glasses. The method is summarized in Appendix B. To avoid zero modes, we include a small staggered field of magnitude ϵ and take the limit $\epsilon \rightarrow 0$.

In Fig. 7 we show the correction to the classical Néel state in the $1/5$ -expansion as obtained from Eq. (B6). Due to the absence of translation symmetry in the lattices, the corrections are site-dependent. The left panels show the average correction within the bulk $\langle \hat{b}_i^\dagger \hat{b}_i \rangle_b$, where we defined the bulk as the $n_l - 1$ inner layers, and the right panels show the maximal correction $\langle \hat{b}_i^\dagger \hat{b}_i \rangle_{\max}$, which can always be found on the sites closest to the angle $\phi = 0$ in the outermost layer and all sites, that can be obtained by performing symmetry-allowed rotations.

As described in Appendix B the limit of $\epsilon \rightarrow 0$ and the thermodynamic limit have to be taken carefully. Taking the limit $\epsilon \rightarrow 0$ on finite lattices leads to divergencies in the correction [Fig. 7] and only in the thermodynamic limit $1/\sqrt{N_s} \rightarrow 0$ the correct results are recovered.

The average corrections in the bulk converge to values smaller than $1/2$ on the largest available lattice sizes for all three lattice geometries [Fig. 7(a)], meaning that the Néel state in the bulk is weakened, but still present in the case of spin 1/2 degrees of freedom. The maximal correction $\langle \hat{b}_i^\dagger \hat{b}_i \rangle_{\max}$ on the other hand side is above $1/2$, such that it is large enough to destroy the magnetic moment on the corresponding sites.

In Fig. 8 the local correction of the {8, 3} lattice with $n_l = 4$ layers at $\epsilon = 0.01$ can be seen. The correction $\langle \hat{b}_i^\dagger \hat{b}_i \rangle$ depends strongly on the coordination number of the corresponding lattice site. In the bulk, where every site has $q = 3$ neighbors, the correction is small. In the edge layer most sites are connected to only two neighboring sites, forming short one-dimensional sections. Therefore the correction on a given site is larger the greater

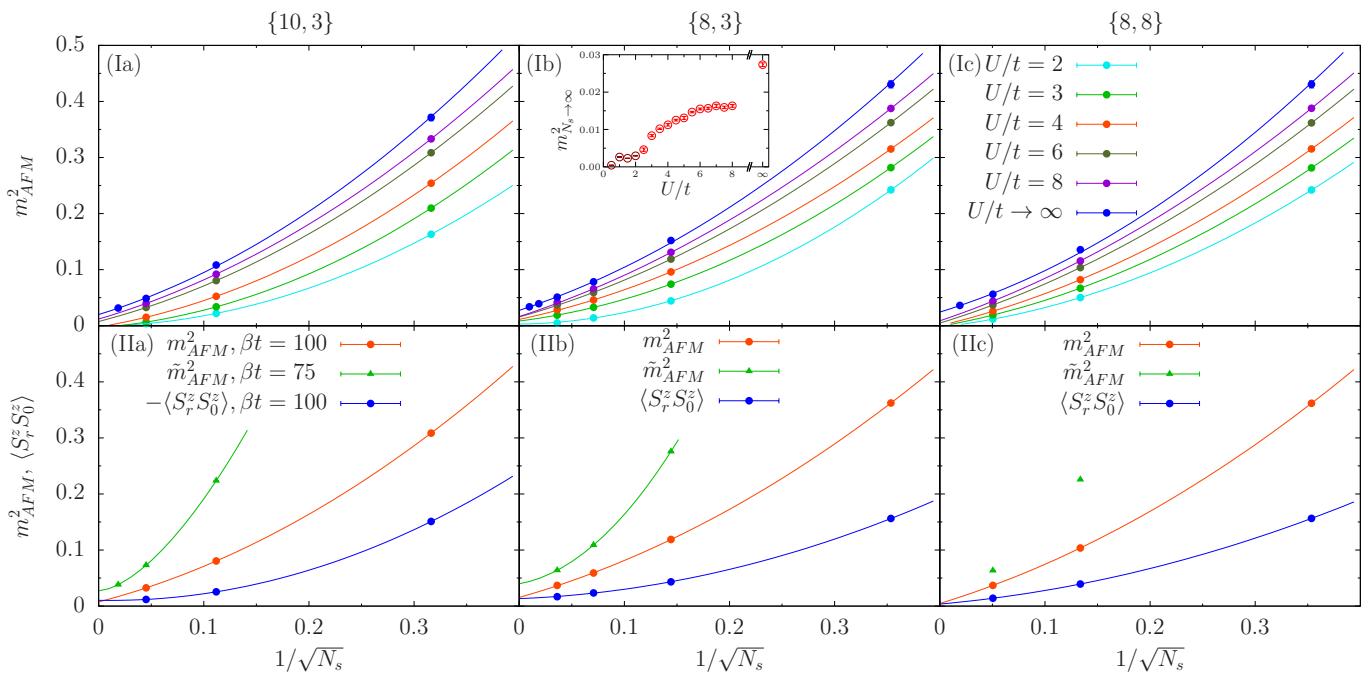


FIG. 9. (Ia)-(Ic) Finite-size scaling of the square of the AFM magnetization (order parameter), defined in Eq. (11), at $\beta t = 100$ for different values of U/t on the $\{10, 3\}$, $\{8, 3\}$ and $\{8, 8\}$ lattice respectively (from left to right). On the x axis we plot the square root of the inverse number of lattice sites N_s . The data points are extrapolated to $N_s \rightarrow \infty$ by a polynomial fit of second order and presented as a function of U/t in the inset. We only present the extrapolated value for the $\{8, 3\}$ lattice, since we have four data points to carry out the fit. We estimate that the systematic error is of the order of 0.005 such that data points below this threshold should be interpreted with care. The data points for $U \rightarrow \infty$ refer to the Heisenberg model at $\beta J = 100$, calculated by SSE. (IIa)-(IIc) Comparison of the squared magnetization, the squared magnetization of the bulk \tilde{m}_{AFM}^2 and the spin-spin correlation $\langle S_r^z S_0^z \rangle$ of two sites with the largest distance to each other on the respective lattice, where S_0^z is the site closest to $\phi = 0$ (for the $\{10, 3\}$ -lattice this is negative since opposing sites lie on different sublattices). Here, we use $U/t = 6$.

the distance to the nearest site with $q = 3$ neighbors. This result is consistent with the absence of long-range order in one dimension, as predicted by spin wave theory. Similar qualitative observations for the other lattice geometries can be found in Fig. 16 of Appendix D 2.

2. Quantum Monte Carlo

The aim of this section is to use numerically exact approaches, AFQMC and SSE, to check the validity of the above statements.

Figures 9(Ia)-9(Ic) plot the staggered spin-spin correlations as defined in Eq. (11) as a function of $\frac{1}{\sqrt{N_s}}$. Unless mentioned otherwise, we consider a finite, but low temperature scale $\beta t = 100$ and fit the data to the form $m_{N_s \rightarrow \infty}^2 + aN_s^{-\frac{1}{2}} + bN_s^{-1}$. It is notoriously hard to extrapolate the staggered magnetization to the thermodynamic limit. First, since the number of sites grow rapidly with n_l we only have a limited set of data. Second, we measure the square of the order parameter such that when the staggered magnetization is small (i.e. at weak coupling or in the proximity of a quantum phase transition) very large lattices are required to obtain reliable results. We note that a pinning field approach [48] that was used

for the Hubbard model on the honeycomb lattice may be an alternative and promising method for future investigations.

For the $\{10, 3\}$ and $\{8, 3\}$ lattices [Figs. 9(Ia) and 9(Ib)] our data at $\beta t = 100$ ($\beta J = 100$) is representative of the ground-state properties for the considered values of n_l . For the $\{8, 3\}$ lattice ordering sets in at $U_c \simeq 2t$. Upon inspection we see that the $\{10, 3\}$ lattice is still disordered at $U/t = 3$. Hence, the trends in the value of U_c , ($U_c^{\{10,3\}} > U_c^{\{8,3\}}$) between the two lattices match our mean-field analysis. It is beyond the scope of this article to determine critical exponent of the order parameter: $m \simeq (U - U_c)^\beta$. In Figs. 9(Ia) and 9(Ib), we equally consider the Heisenberg model. For this model, the SSE allows us to reach much larger lattices such that the extrapolation is more robust.

In Fig. 9(Ic) we consider the flat band system $\{8, 8\}$. With the fermion QMC we can only access three system sizes for the extrapolation. Hence, we do not attempt to determine $m_{N_s \rightarrow \infty}^2$ for this lattice. Furthermore, temperature effects are much larger for this flat band system. Nevertheless, the data is consistent with ordering at large values of U/t and for the Heisenberg model.

In Figs. 9(IIa)-9(IIc), we also present the AFM magnetization of the bulk \tilde{m}_{AFM}^2 by only summing over sites of

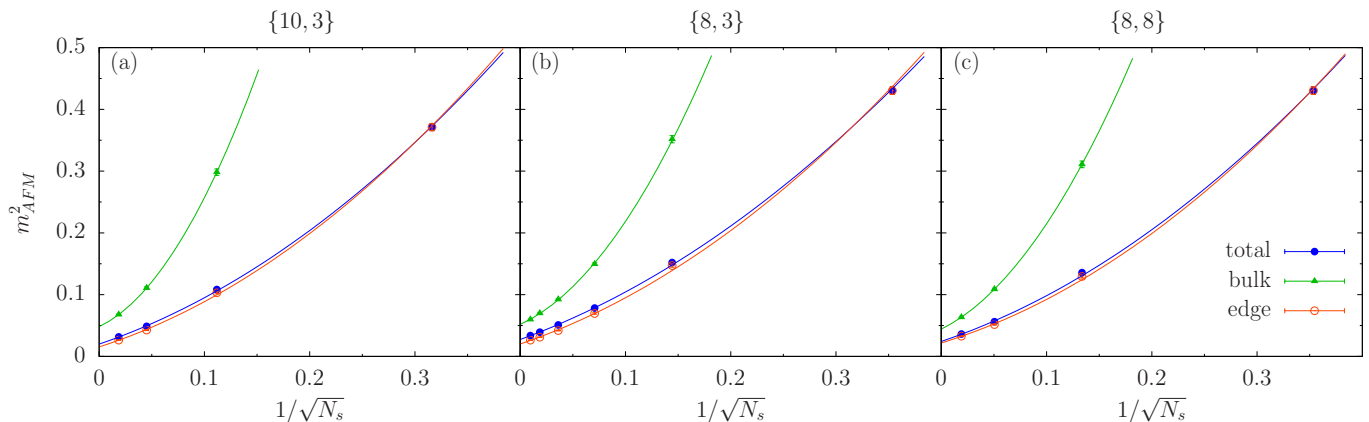


FIG. 10. SSE calculated squared magnetization of the $\{10, 3\}$, $\{8, 3\}$ and $\{8, 8\}$ lattice respectively (from left to right), at $\beta J = 100$, together with the bulk and edge contribution. The data points were fitted with a second order polynomial.

the $n_l - 1$ inner layers. The bulk magnetization is larger than the total magnetization including the edge, consistent with our results from spin wave theory. This becomes more obvious when we consider the bulk and edge contribution to the magnetization calculated by SSE, as presented in Fig. 10. This method allows a more accurate study of the magnetization in the strong-coupling limit as larger lattices can be simulated. While the edge magnetization is slightly lower than the total magnetization, the bulk contribution is larger by a factor of approximately $\sqrt{2}$ for all considered lattices. This specifies our findings from spin wave theory that fluctuations are enhanced on the boundary. The SSE calculations suggest more precisely, that there is still long range order on the edge. Finally, we note that due to the sub-extensiveness of the bulk, the magnetization is determined by the edge contribution. This is supported by the SSE data of Fig. 10 where the total and edge data scale to the same value in

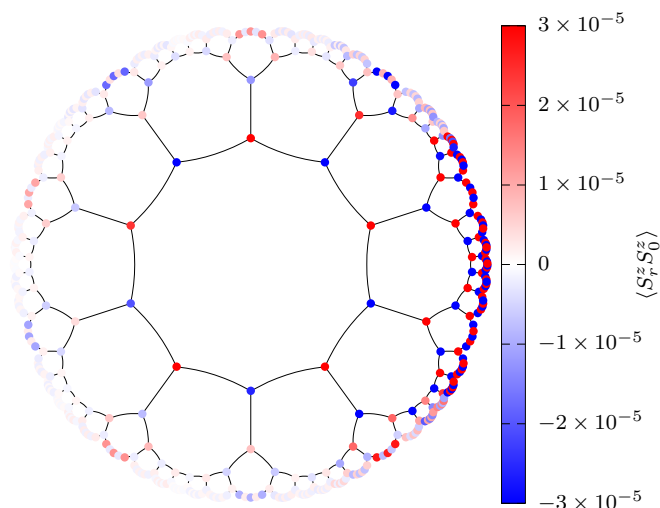


FIG. 11. Spin correlations $\langle S_r^z S_0^z \rangle$ of the $\{10, 3\}$ lattice for $n_l = 3$ layers calculated by AFQMC at $U = 1t$ and $\beta t = 100$. As reference point S_0^z we chose the site closest to $\phi = 0$.

the large n_l limit.

The global AFM is a weak-coupling effect, such that we use the Hubbard model and AFQMC for investigations. To compare the results from mean-field with QMC, we present spin correlations plotted in the Poincaré disk of the $\{10, 3\}$ lattice as shown in Fig. 11. Again considering the weak-coupling regime, similar patterns of alternating positive and negative correlations can be observed in the third layer. This can be directly compared to the mean-field results of the order parameter for the $\{10, 3\}$ lattice in Fig. 13(a), see Appendix. For the presentation of the QMC results, we choose the $\{10, 3\}$ lattice, since it offers the clearest visualization of the observed effect. Note that the considered value of U/t is smaller than the estimated U_c . Nevertheless, the observed spin fluctuations support the notion that in the symmetry-broken phase at large U/t the C_{10} and time-reversal symmetry are broken, but $C_{10}\mathcal{T}$ remains a symmetry of the state.

In order to support the mean-field observation that the system is in an AFM Mott insulating state for strong electronic correlations, we present the spin and charge susceptibility for $U = 5t$ on the $\{10, 3\}$, $\{8, 3\}$ and $\{8, 8\}$ lattice in Figs. 12(Ia)-12(Ic) and 12(IIa)-12(IIc) respectively. As expected for an AFM state spin waves lead to a spin susceptibility χ_S that converges to a finite value as $T \rightarrow 0$. The data shows that there is a buildup of low energy states as one increases n_l . On the other hand, the charge susceptibility χ_C decays exponentially, as expected for a charged, gaped system. Figures 12(IIa)-12(IIc) show that as n_l grows the charge susceptibility remains activated in the low-temperature limit.

V. DISCUSSION AND CONCLUSION

The physics of the half-filled Hubbard and Heisenberg models on bipartite lattices has been investigated in great details for Bravais lattices. Owing to a theorem by Lieb [51], the ground state on a finite lattice is a spin singlet. The lowest energy state in each total spin sector

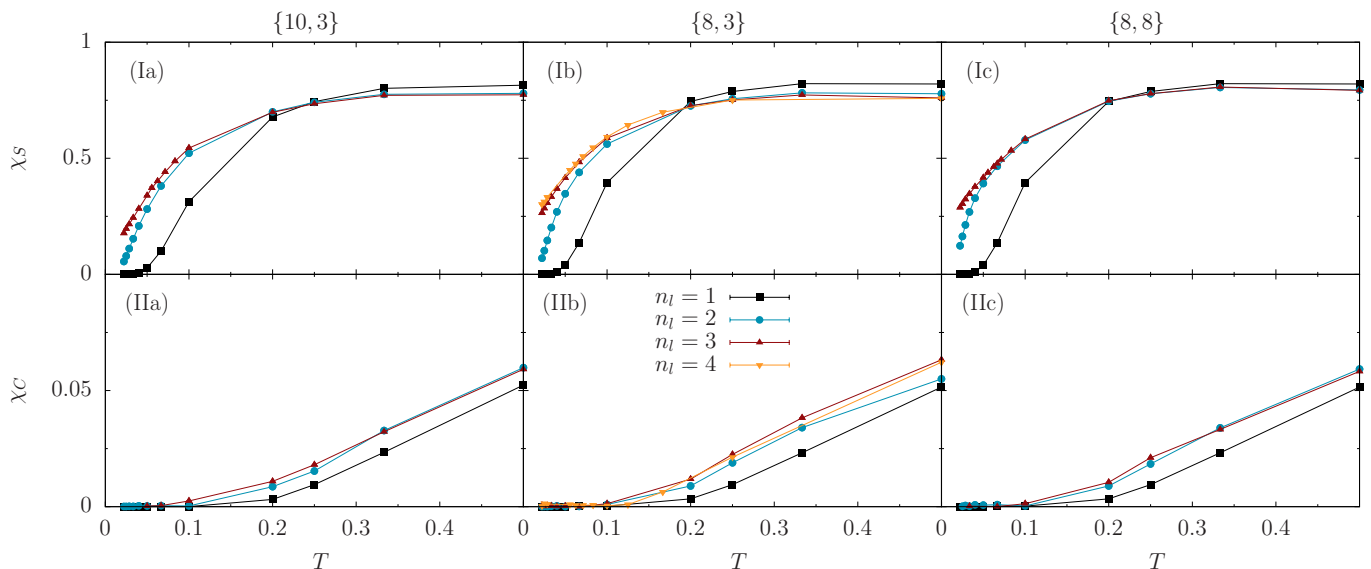


FIG. 12. QMC data for the (Ia)-(Ic) uniform spin susceptibility χ_S and (IIa)-(IIc) charge susceptibility χ_C at $U = 5t$ on the $\{10, 3\}$, $\{8, 3\}$ and $\{8, 8\}$ lattice respectively (from left to right).

builds the Anderson tower of states [67], that collapses in the thermodynamic limit. This is the mechanism that allows for the broken-symmetry quantum AFM ground state without violating the aforementioned Lieb theorem in dimensions greater or equal to two. In one dimension, the Heisenberg and Hubbard models, are critical and are described by an $SO(4)$ Wess-Zumino-Witten theory.

The notion of thermodynamic limit for the hyperbolic lattices differs from the Euclidean case: for the hyperbolic lattices the boundary dominates over the bulk. As a consequence, the very notion of dimensionality and role of fluctuations can be questioned. While our mean-field calculations for the Hubbard model show long-range order on the boundary and in the bulk, a spin wave calculation for the Heisenberg model shows that fluctuations inhibit order at the boundary. As demonstrated by our QMC simulations for both the strong-coupling Hubbard and Heisenberg models, this turns out to be an artifact of the spin wave approximation. It is known that spin waves fail to predict that weakly coupling chains with non-frustrating interactions is a relevant perturbation [68] that leads to long range magnetic order. However, even if the ground state is ordered, it would be of interest to investigate the spin dynamical response on the boundary, with the aim to assess whether proximity to one-dimensional physics is visible at high frequencies as in Ref. [68].

Another direction of research is to consider frustration. It is known that weak frustrating couplings between chains do not necessarily lead to magnetic ordering [69], thereby offering the possibility of realizing different phases in the bulk and on the boundary of hyperbolic lattices.

As for the honeycomb lattice, the Dirac-like character of the DOS close to the Fermi level of the $\{10, 3\}$ and

$\{8, 3\}$ lattices lead to a finite critical interaction strength U_c for the onset of AFM ordering. At the mean-field level the order parameter exponent takes the value $\beta = 1$ as for the Euclidean case. On Euclidean lattices, great progress has been achieved in the understanding of the Gross-Neveu transition, by using renormalization group invariant quantities and finite size scaling to analyze the data [47–49]. For the hyperbolic lattices our analysis is very rudimentary due to the very difficulty of defining a continuum limit and the accompanying critical theory. We find this to be an interesting line of future research. Nevertheless, our data is consistent with a finite- U Mott transition.

The thermodynamic properties of the AFM Mott insulating state are the very same as in the Euclidean case. At low temperatures and in the large n_l limit, the charge susceptibility is activated and the spin susceptibility constant. We note that the notion of Goldstone modes is a property of the symmetry group and not of the lattice structure. As such it is not surprising to observe a finite spin susceptibility in the low-temperature limit.

In the weak-coupling limit patterns of global AFM occur and can be observed in both mean-field and QMC results. Following the probability distribution of the low-lying energy eigenstates, macroscopic ferromagnetic moments are formed, that are compensated in sum. These patterns all have in common, that they break the C_p (down to $C_{p/2}$) and time-reversal symmetry of the Hamiltonian. Additionally the magnetic patterns are invariant under a combination of the original rotation group of the lattice and time-reversal symmetry $C_p \mathcal{T}$. Global AFM occurs e.g. also in finite graphene samples with zig-zag edges [70–76] or in more complex pattern, when the sample is subject to a strain [63, 77, 78].

The absence of negative sign problem in QMC simula-

tions hinges on symmetries (e.g. combined time-reversal and a U(1) conservation) [79, 80] that are not broken by the hyperbolic geometry. Hence all models that are amenable to negative sign-free QMC simulations such as SU(N) Hubbard-Heisenberg models [81], SU(N) Kondo lattices [61, 82], and Su-Schrieffer-Heeger Hamiltonians [83, 84] can be studied. It remains to be seen if novel phenomena can be observed due the hyperbolic geometry.

ACKNOWLEDGMENTS

The authors thank Igor Boettcher and Ronny Thomale for discussions. Special thanks to Igor Boettcher for providing a Mathematica notebook that generates adjacency matrices for hyperbolic lattices. The authors gratefully acknowledge the Gauss Centre for Supercomputing e.V. (www.gauss-centre.eu) for funding this project by providing computing time on the GCS Supercomputer SuperMUC-NG at the Leibniz Supercomputing Centre (www.lrz.de). FA and JI thank the Würzburg-Dresden Cluster of Excellence on Complexity and Topology in Quantum Matter ct.qmat (EXC 2147, project-id 390858490), GR and AG the DFG funded SFB 1170 on Topological and Correlated Electronics at Surfaces and Interfaces. FA acknowledges financial support from the German Research Foundation (DFG) under the grant AS 120/16-1 (Project number 493886309) that is part of the collaborative research project SFB Q-M&S funded by the Austrian Science Fund (FWF) F 86.

Appendix A: Lattice sizes

Table I summarizes the lattices used in the main text and their respective number of lattice sites N_s as a function of the number of layers n_l .

	{10, 3}	{8, 3}	{8, 8}
$n_l = 1$	10	8	8
2	80	48	56
3	490	200	392
4	2880	768	2744
5	16810	2888	
6		10800	

TABLE I. Number of lattice sites for considered lattice geometries as a function of the number of layers n_l .

Appendix B: Spin wave approximation

In this section we briefly outline the calculation of the correction to the classical Néel state within the spin wave

approximation. Since the lattices do not possess translation symmetry, we choose an ansatz for the calculation along the lines of Refs. [65, 66]. Inserting the ansatz of Eqs. (8) and (9) into the Heisenberg Hamiltonian Eq. (7) yields

$$\hat{H} = S \sum_i z_i \hat{b}_i^\dagger \hat{b}_i + \frac{S}{2} \sum_{i,j} T_{i,j} (\hat{b}_i \hat{b}_j + \hat{b}_i^\dagger \hat{b}_j^\dagger) - S^2 N_b. \quad (\text{B1})$$

Here we defined the site-dependent coordination number $z_i = \sum_j T_{i,j}$. We can write the equations of motions for the boson operators in a matrix representation as

$$\frac{d}{dt} \hat{\mathbf{b}} = i \begin{pmatrix} -P & -Q \\ \bar{Q} & \bar{P} \end{pmatrix} \hat{\mathbf{b}} \quad (\text{B2})$$

with

$$\begin{aligned} \hat{\mathbf{b}}^\dagger &= (\hat{b}_{i=1}^\dagger, \dots, \hat{b}_{i=N}^\dagger, \hat{b}_{i=1}, \dots, \hat{b}_{i=N}), \\ P_{i,j} &= S z_i \delta_{i,j}, \quad Q_{i,j} = S T_{i,j}. \end{aligned} \quad (\text{B3})$$

In order to diagonalize the Hamiltonian of Eq. (B1) we perform a Bogoliubov transformation

$$\begin{pmatrix} -\Omega & 0 \\ 0 & \Omega \end{pmatrix} = \begin{pmatrix} \bar{g} & f \\ \bar{f} & g \end{pmatrix}^{-1} \begin{pmatrix} -P & -Q \\ \bar{Q} & \bar{P} \end{pmatrix} \begin{pmatrix} \bar{g} & f \\ \bar{f} & g \end{pmatrix}. \quad (\text{B4})$$

To ensure, that the new boson operators \hat{d}_i^\dagger , that we obtain from $\hat{b}_i^\dagger = \bar{f}_{i,j} \hat{d}_j + g_{i,j} \hat{d}_j^\dagger$, still fulfill the canonical commutation relations, we need to impose a condition on the entries of f and g

$$\begin{pmatrix} \bar{g} & f \\ \bar{f} & g \end{pmatrix} \begin{pmatrix} -1 & 0 \\ 0 & 1 \end{pmatrix} \begin{pmatrix} \bar{g} & f \\ \bar{f} & g \end{pmatrix}^\dagger = \begin{pmatrix} -1 & 0 \\ 0 & 1 \end{pmatrix}. \quad (\text{B5})$$

We now define a scalar product $\langle \mathbf{x}, \mathbf{y} \rangle_B = \mathbf{x}^\dagger \begin{pmatrix} -1 & 0 \\ 0 & 1 \end{pmatrix} \mathbf{y}$. The matrix $M = \begin{pmatrix} -P & -Q \\ \bar{Q} & \bar{P} \end{pmatrix}$ is hermitian with respect to this scalar product $\langle M\mathbf{x}, \mathbf{y} \rangle_B = \langle \mathbf{x}, M\mathbf{y} \rangle_B$ and the Bogoliubov transformation $U = \begin{pmatrix} \bar{g} & f \\ \bar{f} & g \end{pmatrix}$ is unitary $\langle U\mathbf{x}, U\mathbf{y} \rangle_B = \langle \mathbf{x}, \mathbf{y} \rangle_B$. After diagonalizing the matrix M , the condition on the Bogoliubov transformation of Eq. (B5) can be satisfied by ensuring, that all eigenvectors of M are orthonormal with respect to the scalar product $\langle \cdot, \cdot \rangle_B$. If the norm of an eigenvector $\langle \mathbf{x}_n, \mathbf{x}_n \rangle_B > 0$ is nonzero, it can also be shown, that the corresponding eigenvalue is real. In order to avoid eigenvectors with a vanishing B norm we add an infinitesimal staggered magnetic field $\hat{H}_\epsilon = -\epsilon \sum_i (-1)^i \hat{S}_i^z$. After the calculation, limits have to be taken carefully, by first taking the thermodynamic limit and then the limit of $\epsilon \rightarrow 0$. The site-dependent correction to the classical AFM state can be calculated by the mean boson occupation number at $T = 0$

$$\langle \hat{S}_i^z \rangle = S - \langle \hat{b}_i^\dagger \hat{b}_i \rangle = S - \sum_j |f_{i,j}|^2. \quad (\text{B6})$$

Appendix C: Spin susceptibility

In this appendix we show that the assumption of partial particle-hole symmetry and a finite DOS at the Fermi surface, suffices to argue a logarithmic divergence of the staggered spin susceptibility. This calculation does not depend on the lattice symmetry and would also hold for disordered systems where the disorder does not break the said symmetry. The tight-binding part of the Hamiltonian is invariant under a partial particle-hole transformation defined as

$$\hat{P}_\sigma^{-1} \hat{c}_{i,\sigma'}^\dagger \hat{P}_\sigma = \delta_{\sigma,\sigma'} (-1)^i \hat{\gamma}_{i,\sigma'} + (1 - \delta_{\sigma,\sigma'}) \hat{\gamma}_{i,\sigma'}^\dagger. \quad (\text{C1})$$

Without loss of generality we can consider the staggered spin susceptibility in x -direction

$$\begin{aligned} \chi^x(Q) &= \frac{1}{N_s} \int_0^\beta d\tau \sum_{i,j} (-1)^{i+j} \langle \hat{S}_i^x(\tau) \hat{S}_j^x \rangle \quad (\text{C2}) \\ &= \frac{2}{N_s} \int_0^\beta d\tau \sum_{i,j} \langle \hat{\gamma}_{i,\uparrow}^\dagger(\tau) \hat{\gamma}_{j,\uparrow} \rangle \langle \hat{\gamma}_{i,\downarrow}^\dagger(\tau) \hat{\gamma}_{j,\downarrow} \rangle. \end{aligned}$$

As apparent, the partial particle-hole transformation maps the staggered susceptibility in the particle-hole channel to the uniform one in the particle-particle channel. The latter is nothing but the Cooper instability, that we now show to be present on any graph with finite DOS at the Fermi energy. To do so, we introduce a canonical transformation U , that diagonalizes the Hamiltonian

$$\hat{H}_t = \sum_{i,j,\sigma} h_{i,j} \hat{\gamma}_{i,\sigma}^\dagger \hat{\gamma}_{j,\sigma} = \sum_x \lambda_x \hat{\eta}_{x,\sigma}^\dagger \hat{\eta}_{x,\sigma} \quad (\text{C3})$$

with new fermionic operators $\hat{\eta}_{x,\sigma}^\dagger = \sum_i \hat{\gamma}_{i,\sigma}^\dagger U_{i,x}$. Applying this transformation yields

$$\begin{aligned} \chi^x(Q) &= \frac{2}{N_s} \int_0^\beta d\tau \quad (\text{C4}) \\ &\times \sum_{x,y} f_{x,y} e^{\tau(\lambda_x + \lambda_y)} \langle \hat{\eta}_{x,\uparrow}^\dagger \hat{\eta}_{x,\uparrow} \rangle \langle \hat{\eta}_{y,\downarrow}^\dagger \hat{\eta}_{y,\downarrow} \rangle \\ &= \frac{1}{N_s} \sum_{x,y} \frac{f_{x,y}}{\lambda_x + \lambda_y} \left[\tanh\left(\frac{\beta}{2}\lambda_x\right) + \tanh\left(\frac{\beta}{2}\lambda_y\right) \right] \end{aligned}$$

with $f_{x,y} = \sum_{i,j} (U^\dagger)_{x,i} U_{j,x} (U^\dagger)_{y,i} U_{j,y}$. If the DOS is finite at zero energy, the Fermi level here, we can show, that the term with $x = y$ has a logarithmic divergency

$$\begin{aligned} \chi^x(Q) &= \frac{1}{N_s} \sum_x \frac{f_{x,x}}{\lambda_x} \tanh\left(\frac{\beta}{2}\lambda_x\right) + R \\ &= \int d\epsilon \rho(\epsilon) \frac{1}{\epsilon} \tanh\left(\frac{\beta}{2}\epsilon\right) + R \\ &\approx \rho(0) \ln\left(\frac{W}{2k_b T}\right) + R, \quad (\text{C5}) \end{aligned}$$

where all other terms in the sum with $x \neq y$ are summarized in the term R . The last approximation is in

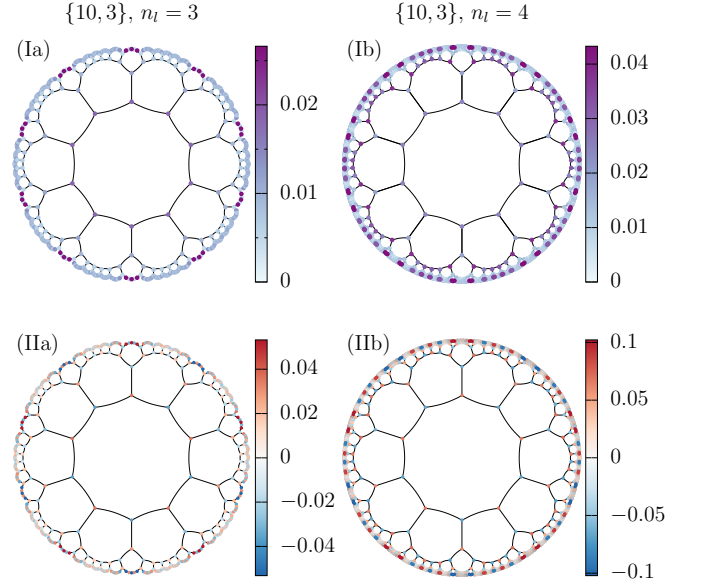


FIG. 13. (I) Local DOS $\rho(E=0, \mathbf{i})$ at zero energy in the non-interacting limit $U=0$ at $\delta=0.01$ and (II) magnetization m_i^z as obtained from mean-field approximation for the $\{10,3\}$ lattice and interaction strength $U=0.8t$.

the low-temperature limit and W is a high-energy cutoff. In principle terms could appear in R , that lead to the cancellation of the logarithmic divergency under certain conditions. But in general the occurrence of an instability towards AFM ordering is generic even in the absence of translational symmetry.

Appendix D: Additional data

In the following section we present some additional data.

1. Mean-field approximation

In Sec. IV B we showed the spatial distribution of the magnetization m_i^z in the weak-coupling limit for the $\{8,3\}$ lattice with $n_l=5$ layers. In the upper panels of Figs. 13-15 we plot the local DOS at zero energy

$$\rho(E, \mathbf{i}) = -\frac{1}{\pi N_s} \sum_n |U_{i,n}|^2 \text{Im} G^R(n, E) \quad (\text{D1})$$

for the different lattice geometries both with $n_l=3$ and $n_l=4$ layers. Here we defined a canonical transformation U , that diagonalizes the mean-field Hamiltonian (4). They all show a unique pattern of low and high DOS, that is compatible with the C_p symmetry of the lattices. The lower panels of Figs. 13-15 show the corresponding local order parameter in real-space, where again local ferromagnetic and AFM moments emerge in the differ-

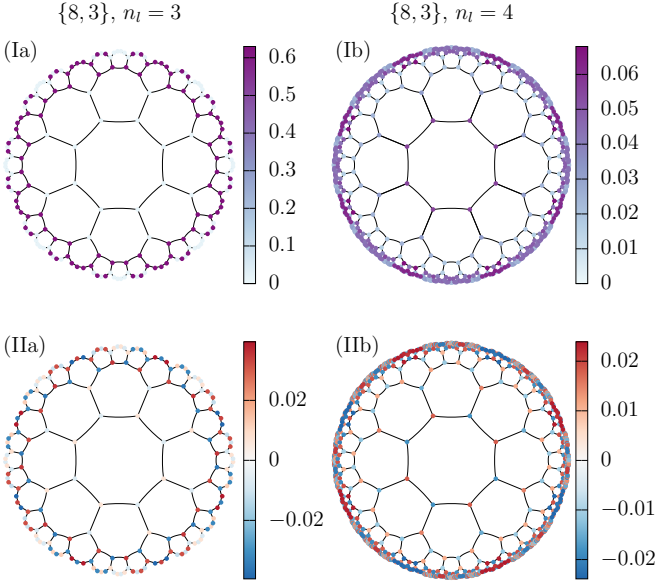


FIG. 14. Same as in Fig. 13, but for the $\{8,3\}$ lattice and interaction strength (IIa) $U = 0.4t$ and (IIb) $U = 0.58t$.

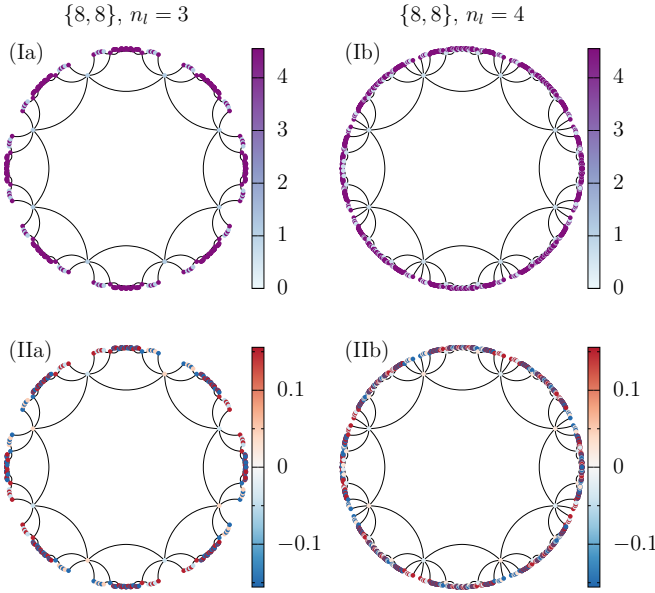


FIG. 15. Same as in Fig. 13, but for the $\{8,8\}$ lattice and interaction strength $U = 0.1t$.

ent sectors of the lattice. But in sum of all lattice sites only the AFM moment remains.

2. Spin wave approximation

The results for the site-dependent correction $\langle \hat{b}_i^\dagger \hat{b}_i \rangle$ to the classical Néel state obtained from the spin wave approximation for the $\{10,3\}$ and $\{8,3\}$ lattice in Figs. 16(I) and 16(II) are similar to the results for the $\{8,3\}$ lattice described in the main text [Fig. 8]. For the

$\{8,8\}$ lattice the results differ slightly due to the lattice geometry. The correction on many sites in the outermost layer is smaller than for the other two lattices, since the distance from one site on the edge to another site on the edge is in general smaller. This is a consequence of the high coordination number $q = 8$, since sites in the bulk can have direct connections to the edge. The sites on the edge also form short one-dimensional chains, but larger effective interactions are present in comparison to the other two considered lattice geometries.

3. Quantum Monte Carlo

In order to supplement the picture given in Figs. 9 and 11, we present the order parameter m_{AFM}^z as a function of U in Fig. 17 for two different temperatures $\beta t = 25$ and $\beta t = 100$. We see that the $\{8,8\}$ lattice exhibits stronger temperature effects than the other lattices. This lattice shows a strong sensitivity to temperature already in the weak coupling regime, as can be seen in Fig. 17(c). As discussed before, this effect is also present in the results from a mean-field analysis [Fig. 4(a)].

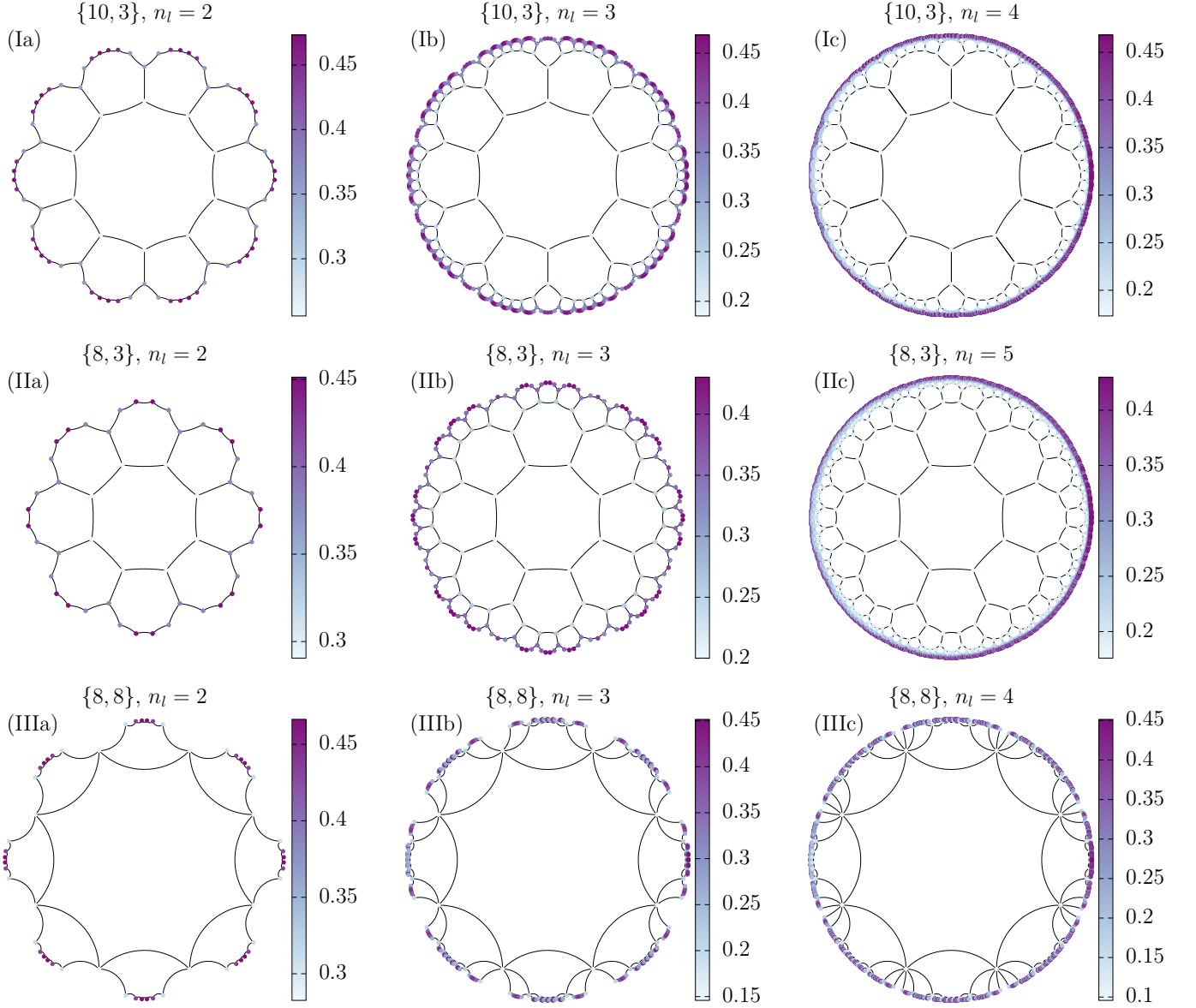


FIG. 16. Local correction $\langle \hat{b}_i^\dagger \hat{b}_i \rangle$ to classical Néel state as obtained from spin wave approximation for the (I) $\{10, 3\}$, (II) $\{8, 3\}$ and (III) $\{8, 8\}$ lattice and varying system size n_l at $\epsilon = 0.01$.

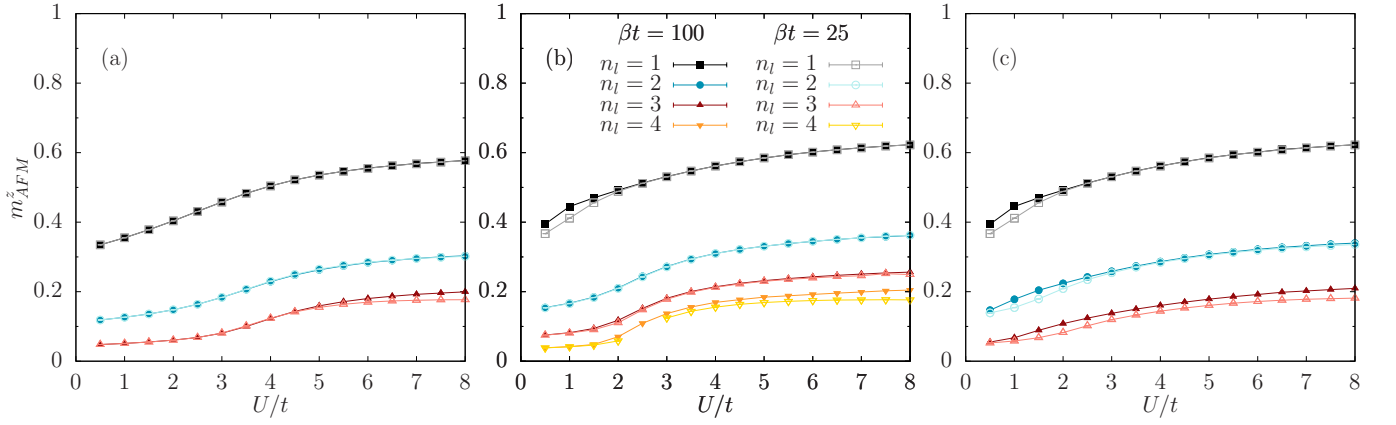


FIG. 17. AFM order parameter for the $\{10,3\}$, $\{8,3\}$ and $\{8,8\}$ lattice obtained by QMC calculations at $\beta t = 100$ (filled symbols) and $\beta t = 25$ (unfilled symbols).

-
- [1] C. C. Wu, Ising models on hyperbolic graphs, *Journal of Statistical Physics* **85**, 251 (1996).
- [2] C. C. Wu, Ising models on hyperbolic graphs ii, *Journal of Statistical Physics* **100**, 893 (2000).
- [3] H. Shima and Y. Sakaniwa, Geometric effects on critical behaviours of the ising model, *Journal of Physics A: Mathematical and General* **39**, 4921 (2006).
- [4] H. Shima and Y. Sakaniwa, The dynamic exponent of the ising model on negatively curved surfaces, *Journal of Statistical Mechanics: Theory and Experiment* **2006**, P08017 (2006).
- [5] K. Ueda, R. Kremer, A. Gendiar, and T. Nishino, Corner transfer matrix renormalization group method applied to the ising model on the hyperbolic plane, *Journal of the Physical Society of Japan* **76**, 084004 (2007), <https://doi.org/10.1143/JPSJ.76.084004>.
- [6] Y. Sakaniwa and H. Shima, Survival of short-range order in the ising model on negatively curved surfaces, *Phys. Rev. E* **80**, 021103 (2009).
- [7] M. Daniška and A. Gendiar, Analysis of quantum spin models on hyperbolic lattices and bethe lattice, *Journal of Physics A: Mathematical and Theoretical* **49**, 145003 (2016).
- [8] N. P. Breuckmann, B. Placke, and A. Roy, Critical properties of the ising model in hyperbolic space, *Phys. Rev. E* **101**, 022124 (2020).
- [9] I. Benjamini, R. Lyons, Y. Peres, and O. Schramm, Critical Percolation on Any Nonamenable Group has no Infinite Clusters, *The Annals of Probability* **27**, 1347 (1999).
- [10] I. Benjamini and O. Schramm, Percolation in the hyperbolic plane, *Journal of the American Mathematical Society* **14**, 487 (2001).
- [11] S. K. Baek, P. Minnhagen, and B. J. Kim, Percolation on hyperbolic lattices, *Phys. Rev. E* **79**, 011124 (2009).
- [12] C. G. Callan and F. Wilczek, Infrared behavior at negative curvature, *Nuclear Physics B* **340**, 366 (1990).
- [13] A. J. Kollár, M. Fitzpatrick, P. Sarnak, and A. A. Houck, Line-graph lattices: Euclidean and non-euclidean flat bands, and implementations in circuit quantum electrodynamics, *Communications in Mathematical Physics* **376**, 1909 (2020).
- [14] S. Yu, X. Piao, and N. Park, Topological hyperbolic lattices, *Phys. Rev. Lett.* **125**, 053901 (2020).
- [15] I. Boettcher, P. Bienias, R. Belyansky, A. J. Kollár, and A. V. Gorshkov, Quantum simulation of hyperbolic space with circuit quantum electrodynamics: From graphs to geometry, *Phys. Rev. A* **102**, 032208 (2020).
- [16] J. Maciejko and S. Rayan, Hyperbolic band theory, *Science Advances* **7**, eabe9170 (2021), <https://www.science.org/doi/pdf/10.1126/sciadv.abe9170>.
- [17] K. Ikeda, S. Aoki, and Y. Matsuki, Hyperbolic band theory under magnetic field and dirac cones on a higher genus surface, *Journal of Physics: Condensed Matter* **33**, 485602 (2021).
- [18] J. Maciejko and S. Rayan, Automorphic bloch theorems for hyperbolic lattices, *Proceedings of the National Academy of Sciences* **119**, e2116869119 (2022), <https://www.pnas.org/doi/pdf/10.1073/pnas.2116869119>.
- [19] I. Boettcher, A. V. Gorshkov, A. J. Kollár, J. Maciejko, S. Rayan, and R. Thomale, Crystallography of hyperbolic lattices, *Phys. Rev. B* **105**, 125118 (2022).
- [20] A. Stegmaier, L. K. Upreti, R. Thomale, and I. Boettcher, Universality of hofstadter butterflies on hyperbolic lattices, *Phys. Rev. Lett.* **128**, 166402 (2022).
- [21] W. Zhang, H. Yuan, N. Sun, H. Sun, and X. Zhang, Observation of novel topological states in hyperbolic lattices, *Nature Communications* **13**, 2937 (2022).
- [22] Z.-R. Liu, C.-B. Hua, T. Peng, and B. Zhou, Chern insulator in a hyperbolic lattice, *Phys. Rev. B* **105**, 245301 (2022).
- [23] T. Bzdušek and J. Maciejko, Flat bands and band-touching from real-space topology in hyperbolic lattices, *Phys. Rev. B* **106**, 155146 (2022).
- [24] D. M. Urwyler, P. M. Lenggenhager, I. Boettcher, R. Thomale, T. Neupert, and T. Bzdušek, Hyperbolic topological band insulators, *Phys. Rev. Lett.* **129**, 246402 (2022).
- [25] A. Chen, H. Brand, T. Helbig, T. Hofmann, S. Imhof, A. Fritzsche, T. Kießling, A. Stegmaier, L. K. Upreti, T. Neupert, T. Bzdušek, M. Greiter, R. Thomale, and I. Boettcher, Hyperbolic matter in electrical circuits with tunable complex phases, *Nature Communications* **14**, 622 (2023).
- [26] N. Gluscevich, A. Samanta, S. Manna, and B. Roy, Dynamic mass generation on two-dimensional electronic hyperbolic lattices (2023), arXiv:2302.04864 [cond-mat.str-el].
- [27] R. Mosseri and J. Vidal, Density of states of tight-binding models in the hyperbolic plane, *Phys. Rev. B* **108**, 035154 (2023).
- [28] X. Zhu, J. Guo, N. P. Breuckmann, H. Guo, and S. Feng, Quantum phase transitions of interacting bosons on hyperbolic lattices, *Journal of Physics: Condensed Matter* **33**, 335602 (2021).
- [29] P. Bienias, I. Boettcher, R. Belyansky, A. J. Kollár, and A. V. Gorshkov, Circuit quantum electrodynamics in hyperbolic space: From photon bound states to frustrated spin models, *Phys. Rev. Lett.* **128**, 013601 (2022).
- [30] A. J. Kollár, M. Fitzpatrick, and A. A. Houck, Hyperbolic lattices in circuit quantum electrodynamics, *Nature* **571**, 45 (2019).
- [31] P. M. Lenggenhager, A. Stegmaier, L. K. Upreti, T. Hofmann, T. Helbig, A. Vollhardt, M. Greiter, C. H. Lee, S. Imhof, H. Brand, T. Kießling, I. Boettcher, T. Neupert, R. Thomale, and T. Bzdušek, Simulating hyperbolic space on a circuit board, *Nature Communications* **13**, 4373 (2022).
- [32] H. S. M. Coxeter, *Regular Polytopes* (Dover, New York, 1973).
- [33] A. L. Edmonds, J. H. Ewing, and R. S. Kulkarni, Regular tessellations of surfaces and $(p, q, 2)$ -triangle groups, *Annals of Mathematics* **116**, 113 (1982).
- [34] The metric in the hyperbolic plane with a constant negative curvature of -1 is given by $ds^2 = 4 \frac{dx^2 + dy^2}{(1-x^2-y^2)^2}$. Here, x and y are the coordinates within the open unit circle in the Poincaré disk model.
- [35] J. W. Cannon, W. J. Floyd, R. Kenyon, and W. R. Parry, *Flavors of geometry* (Cambridge University Press, Cambridge, 1997) Chap. Hyperbolic Geometry, pp. 59–115.
- [36] J. W. Anderson, *Hyperbolic Geometry* (Springer, London, 2005).

- [37] F. Sausset and G. Tarjus, Periodic boundary conditions on the pseudosphere, *Journal of Physics A: Mathematical and Theoretical* **40**, 12873 (2007).
- [38] J. Hubbard, Electron correlations in narrow energy bands, *Proceedings of the Royal Society of London. Series A, Mathematical and Physical Sciences* **276**, 238 (1963).
- [39] M. C. Gutzwiller, Effect of correlation on the ferromagnetism of transition metals, *Phys. Rev. Lett.* **10**, 159 (1963).
- [40] J. Kanamori, Electron Correlation and Ferromagnetism of Transition Metals, *Progress of Theoretical Physics* **30**, 275 (1963), <https://academic.oup.com/ptp/article-pdf/30/3/275/5278869/30-3-275.pdf>.
- [41] J. E. Hirsch, Two-dimensional hubbard model: Numerical simulation study, *Phys. Rev. B* **31**, 4403 (1985).
- [42] E. Fradkin, *Field Theories of Condensed Matter Physics*, 2nd ed. (Cambridge University Press, Cambridge, 2013).
- [43] J. E. Hirsch and S. Tang, Antiferromagnetism in the two-dimensional hubbard model, *Phys. Rev. Lett.* **62**, 591 (1989).
- [44] S. White, D. Scalapino, R. Sugar, E. Loh, J. Gubernatis, and R. Scalettar, Numerical study of the two-dimensional hubbard model, *Phys. Rev. B* **40**, 506 (1989).
- [45] J. P. F. LeBlanc, A. E. Antipov, F. Becca, I. W. Bulik, G. K.-L. Chan, C.-M. Chung, Y. Deng, M. Ferrero, T. M. Henderson, C. A. Jiménez-Hoyos, E. Kozik, X.-W. Liu, A. J. Millis, N. V. Prokof'ev, M. Qin, G. E. Scuseria, H. Shi, B. V. Svistunov, L. F. Tocchio, I. S. Tupitsyn, S. R. White, S. Zhang, B.-X. Zheng, Z. Zhu, and E. Gull (Simons Collaboration on the Many-Electron Problem), Solutions of the two-dimensional hubbard model: Benchmarks and results from a wide range of numerical algorithms, *Phys. Rev. X* **5**, 041041 (2015).
- [46] S. Sorella and E. Tosatti, Semi-metal-insulator transition of the hubbard model in the honeycomb lattice, *Europhysics Letters* **19**, 699 (1992).
- [47] S. Sorella, Y. Otsuka, and S. Yunoki, Absence of a spin liquid phase in the hubbard model on the honeycomb lattice, *Scientific Reports* **2**, 992 (2012).
- [48] F. F. Assaad and I. F. Herbut, Pinning the order: The nature of quantum criticality in the hubbard model on honeycomb lattice, *Phys. Rev. X* **3**, 031010 (2013).
- [49] Y. Otsuka, S. Yunoki, and S. Sorella, Universal quantum criticality in the metal-insulator transition of two-dimensional interacting dirac electrons, *Phys. Rev. X* **6**, 011029 (2016).
- [50] I. F. Herbut, Interactions and phase transitions on graphene's honeycomb lattice, *Phys. Rev. Lett.* **97**, 146401 (2006).
- [51] E. H. Lieb, Two theorems on the hubbard model, *Phys. Rev. Lett.* **62**, 1201 (1989).
- [52] P. W. Anderson, New approach to the theory of superexchange interactions, *Phys. Rev.* **115**, 2 (1959).
- [53] T. Holstein and H. Primakoff, Field dependence of the intrinsic domain magnetization of a ferromagnet, *Phys. Rev.* **58**, 1098 (1940).
- [54] R. Blankenbecler, D. J. Scalapino, and R. L. Sugar, Monte carlo calculations of coupled boson-fermion systems. i, *Phys. Rev. D* **24**, 2278 (1981).
- [55] F. Assaad and H. Evertz, World-line and determinantal quantum monte carlo methods for spins, phonons and electrons, in *Computational Many-Particle Physics, Lecture Notes in Physics*, Vol. 739, edited by H. Fehske, R. Schneider, and A. Weiße (Springer, Berlin Heidelberg, 2008) pp. 277–356.
- [56] A. W. Sandvik and J. Kurkijärvi, Quantum monte carlo simulation method for spin systems, *Physical Review B* **43**, 5950 (1991).
- [57] O. F. Syljuåsen and A. W. Sandvik, Quantum monte carlo with directed loops, *Physical Review E* **66**, 046701 (2002).
- [58] F. F. Assaad, M. Bercx, F. Goth, A. Götz, J. S. Hofmann, E. Huffman, Z. Liu, F. P. Toldin, J. S. E. Portela, and J. Schwab, The ALF (Algorithms for Lattice Fermions) project release 2.0. Documentation for the auxiliary-field quantum Monte Carlo code, *SciPost Phys. Codebases* **1**, 1 (2022).
- [59] O. F. Syljuåsen, Directed loop updates for quantum lattice models, *Physical Review E* **67**, 046701 (2003).
- [60] I. F. Herbut, V. Juričić, and B. Roy, Theory of interacting electrons on the honeycomb lattice, *Phys. Rev. B* **79**, 085116 (2009).
- [61] M. Raczkowski, R. Peters, T. T. Phùng, N. Takemori, F. F. Assaad, A. Honecker, and J. Vahedi, Hubbard model on the honeycomb lattice: From static and dynamical mean-field theories to lattice quantum monte carlo simulations, *Phys. Rev. B* **101**, 125103 (2020).
- [62] M. Bercx, F. Goth, J. S. Hofmann, and F. F. Assaad, The ALF (Algorithms for Lattice Fermions) project release 1.0. Documentation for the auxiliary field quantum Monte Carlo code, *SciPost Phys.* **3**, 013 (2017).
- [63] B. Roy, F. F. Assaad, and I. F. Herbut, Zero modes and global antiferromagnetism in strained graphene, *Phys. Rev. X* **4**, 021042 (2014).
- [64] L. Šmejkal, J. Sinova, and T. Jungwirth, Emerging research landscape of altermagnetism, *Phys. Rev. X* **12**, 040501 (2022).
- [65] L. R. Walker and R. E. Walstedt, Computer model of metallic spin-glasses, *Phys. Rev. B* **22**, 3816 (1980).
- [66] S. Sanyal, A. Banerjee, K. Damle, and A. W. Sandvik, Antiferromagnetic order in systems with doublet $S_{\text{tot}} = \frac{1}{2}$ ground states, *Phys. Rev. B* **86**, 064418 (2012).
- [67] P. W. Anderson, An approximate quantum theory of the antiferromagnetic ground state, *Phys. Rev.* **86**, 694 (1952).
- [68] M. Raczkowski and F. F. Assaad, Spinon confinement: Dynamics of weakly coupled hubbard chains, *Phys. Rev. B* **88**, 085120 (2013).
- [69] O. A. Starykh and L. Balents, Ordering in spatially anisotropic triangular antiferromagnets, *Phys. Rev. Lett.* **98**, 077205 (2007).
- [70] M. Fujita, K. Wakabayashi, K. Nakada, and K. Kusakabe, Peculiar localized state at zigzag graphite edge, *Journal of the Physical Society of Japan* **65**, 1920 (1996), <https://doi.org/10.1143/JPSJ.65.1920>.
- [71] J. Fernández-Rossier and J. J. Palacios, Magnetism in graphene nanoislands, *Phys. Rev. Lett.* **99**, 177204 (2007).
- [72] J. Fernández-Rossier, Prediction of hidden multiferroic order in graphene zigzag ribbons, *Phys. Rev. B* **77**, 075430 (2008).
- [73] S. Bhowmick and V. B. Shenoy, Edge state magnetism of single layer graphene nanostructures, *The Journal of Chemical Physics* **128**, 244717 (2008), https://pubs.aip.org/aip/jcp/article-pdf/doi/10.1063/1.2943678/15416213/244717_1_online.pdf.
- [74] H. Feldner, Z. Y. Meng, A. Honecker, D. Cabra, S. Wessel, and F. F. Assaad, Magnetism of finite graphene sam-

- ples: Mean-field theory compared with exact diagonalization and quantum monte carlo simulations, *Phys. Rev. B* **81**, 115416 (2010).
- [75] O. V. Yazyev, Emergence of magnetism in graphene materials and nanostructures, *Reports on Progress in Physics* **73**, 056501 (2010).
- [76] M. Raczkowski and F. F. Assaad, Interplay between the edge-state magnetism and long-range Coulomb interaction in zigzag graphene nanoribbons: Quantum Monte Carlo study, *Phys. Rev. B* **96**, 115155 (2017).
- [77] J. Viana-Gomes, V. M. Pereira, and N. M. R. Peres, Magnetism in strained graphene dots, *Phys. Rev. B* **80**, 245436 (2009).
- [78] S. Cheng, J. Yu, T. Ma, and N. M. R. Peres, Strain-induced edge magnetism at the zigzag edge of a graphene quantum dot, *Phys. Rev. B* **91**, 075410 (2015).
- [79] C. Wu and S.-C. Zhang, Sufficient condition for absence of the sign problem in the fermionic quantum monte carlo algorithm, *Phys. Rev. B* **71**, 155115 (2005).
- [80] Z.-X. Li, Y.-F. Jiang, and H. Yao, Majorana-time-reversal symmetries: A fundamental principle for sign-problem-free quantum monte carlo simulations, *Phys. Rev. Lett.* **117**, 267002 (2016).
- [81] F. F. Assaad, Phase diagram of the half-filled two-dimensional $SU(n)$ hubbard-heisenberg model: A quantum monte carlo study, *Phys. Rev. B* **71**, 075103 (2005).
- [82] F. F. Assaad, Quantum monte carlo simulations of the half-filled two-dimensional kondo lattice model, *Phys. Rev. Lett.* **83**, 796 (1999).
- [83] A. Götz, S. Beyl, M. Hohenadler, and F. F. Assaad, Valence-bond solid to antiferromagnet transition in the two-dimensional su-schrieffer-heeger model by langevin dynamics, *Phys. Rev. B* **105**, 085151 (2022).
- [84] A. Götz, M. Hohenadler, and F. F. Assaad, Phases and exotic phase transitions of a two-dimensional su-schrieffer-heeger model, *Phys. Rev. B* **109**, 195154 (2024).